Radiocarbon dating of sediments using ramped pyrolysis and its application to the event stratigraphy in the Arctic Ocean

昇温熱分解^{14}C 法による堆積物年代推定と

北極海イベント層の層位学的研究

Graduate School of Environmental Science

Hokkaido University

Kenta Suzuki

北海道大学大学院環境科学院

鈴木健太

TABLE OF CONTENTS

ABSTRACT 5

ACKNOWLEDGMENTS 7

CHAPTER I. General Introduction

1.1. Millennial-scale climate variability during the deglaciation 9

CHAPTER II. Development of Age Estimation Method using the Ramped Pyrolysis ^{14}C Dating

2.1. Introduction 19

2.2. Material and methods

2.2.1. Sediment material 21

2.2.2. Ramped pyrolysis ^{14}C dating 24

2.3. Results 26

2.4. Discussion

2.4.1. The origin of the G1, G2 and G3 components

and their age interpretation 28

2.4.2. Age estimates from RP ^{14}C data 31

2.5. Conclusions 34

CHAPTER III. Event Stratigraphy of Deglacial Sediments in the Western Arctic

3.1. Introduction 50

3.2. Material and methods

3.2.1. The study area 52

3.2.2. Samples 52

3.2.3. Methods 53

3.3. Results

3..3.1. Lithology and color 57

3.3.2. The abundance of >63 μm fraction (IRD abundance) and the grain size distribution of the <63 μm fraction 58

3.3.3. Mineral composition 58

3.3.4. Organic matter 59

3.3.5. GDGTs 59

3.4. Discussion

3.4.1. Stratigraphic correlation based on grain size and mineral composition 59

3.4.2. Provenance of the DK layers 61

3.4.3. The characteristics and provenance of the K layer (=P layer) 62

3.5. Conclusions 65

CHAPTER IV. General Discussion

4.1. Introduction 84

4.2. Methods 85

4.3. Results and discussion 85

4.4. General Summary 89

References 93

ABSTRACT

The Arctic Ocean played a major role in millennial-scale climate changes during the last glacial period. In this study, I identified the vast sediment discharge from the proto-Mackenzie River to the western Arctic in the period between 14,500 and 13,200 years ago (Bølling-Allerød [BA] period) and discussed the paleoclimatic significance of this remarkable event. The application of ramped pyrolysis (RP) ^{14}C dating (Rosenheim et al., 2008) was necessary to date western Arctic sediments. Because RP ^{14}C dates of sedimentary organic matter do not indicate the age of sediments directly, I invented a calibration method of converting RP ^{14}C data-set to sediment age. During ramped pyrolysis, the carbon of gas generated at higher temperatures showed an older age. Based on this empirical relationship between pyrolysis temperature and ^{14}C concentration of generated gas, a new calibration method was proposed to determine the age of sediment within 1600 years (average 460 years) for samples deposited in the past 15,000 years.

Using this newly-developed technique, I determined the ages of sediments retrieved from the western Arctic. The stratigraphy of western Arctic sediments was revised based on the combination of lithological (color, gran size, sorting, and IRD abundance), mineralogical and geochemical (organic carbon, sulfur, nitrogen and glycerol dialkyl glycerol tetraethers [GDGTs]) properties. A characteristic silt layer was widely observed

in the Chukchi Borderland and the Beaufort Sea. The sediment of this layer is rich in kaolinite, fine coal fragments and abundant soil-derived GDGTs, and its provenance is assumed to be inland Canada where the kaolinite and coal-bearing Cretaceous Scholard Formation. RP ^{14}C dating indicated that the ages of bottom and top of this layer are 14,500 and 13,200 years ago, respectively, corresponding the onset and end of the BA period. I thus conclude that this sediment was delivered from inland Canada via the proto-Mackenzie River during the BA period.

Assuming the density of turbid water discharged from the proto-Mackenzie River, I estimated that the total amount of discharged freshwater was $4.3 \times 10^5 \sim 1.3 \times 10^6$ km^3 during the BA period. This corresponds to 5 ~ 14 % of the total discharged water from world ice sheets during the BA period.

ACKNOWLEDGMENTS

I thank Prof. Masanobu Yamamoto for supervising my doctor project. I also thank Dr. Leonid Polyak of Ohio state University for providing sediment core samples, discussion, and supervising my study during my one-year stay in Columbus, Dr. Seung-Il Nam of Korean Polar Institute for providing sediment core samples and discussion, Dr. Tomohisa Irino for his kind instructions of X-ray diffraction and grain size analysis in his laboratory, Prof. Brad E. Rosenheim of University of South Florida for his kind offer of the usage of RP equipment in his laboratory, Dr. Takayuki Omori of University of Tokyo for his kind instructions of ^{14}C dating analysis in his laboratory, and Prof. Toshiro Yamanaka of Tokyo University of Marine Science and Technology for his kind instructions of organic matter analysis in his laboratory. Prof. Atsuko Sugimoto and Prof. Youhei Yamashita are thanked for their kind advice. I also thank Prof. Yoshito Chikaraishi (Hokkaido University) and Dr. Naomi Harada (the Japan Agency for Marine-Earth Science and Technology) for their review of this thesis and giving comments. Special acknowledgments are given to the members of Yamamoto laboratory for helpful assistance.

CHAPTER I.
General Introduction

1.1. Millennial-scale climate variability during the deglaciation

The glacial period is characterized by millennial-scale abrupt climate variability, such as the Dansgaard-Oeschger (DO) cycles (Dansgaard et al., 1993) (Fig. 1-1). The deglaciation was the period characterized by the maximum millennial-scale climate change in the Greenland ice core $\delta^{18}O$ record (Fig. 1-1; Dansgaard et al., 1993, Seierstad et al., 2014). Ice core $\delta^{18}O$ shows that the warm Bølling-Allerød (BA) period started by abrupt warming after cold Older Dryas (OD) period and ended by cooling at the onset of the Younger Dryas (YD) period (Fig. 1-1; e.g. Oeschger et al., 1980; Alley et l., 1993).

Changes in the Atlantic meridional overturning circulation (AMOC) are considered as one of the causes of this millennium-scale climate change. The AOMC is the basin-scale circulation of the Atlantic Ocean water, which is characterized by a combination of a northward flow of surface warm, salty water and a southward deep water flow of colder waters (the North Atlantic Deep Water; NADW). The AMOC is an important component of the Earth's climate system and plays a major role in heat transport to the northern high latitudes (Fig. 1-2; Broecker et al., 1989, Rahmstorf, 1997). The salinity of the surface water of the North Atlantic (Nordic and Labrador Seas) is a key of the regulation of the AMOC (Broecker et al., 1989). Thus, the meltwater inflow from the Laurentide ice sheet is a most likely trigger to change the AMOC during the last glacial and deglacial periods

(Fig. 1-3; Manabe and Stouffer, 1995; Rahmstorf, 2002, 2003; Böhm et al., 2015). Geological evidence indicated that the level of the Lake Agassiz, a huge glacial lake exited along the southern margin of the Laurentide ice sheet during the deglacial, dropped at the onset of the YD (Keigwin et al., 2018). Based on this observation, Broecker et al. (1989) suggested the freshwater discharge from the Lake Agassiz supplied freshwater to the North Atlantic and stopped the formation of the NADW and the AMOC. However, the timing and route of meltwater from the Laurentide ice sheet during the last deglaciation and those effect to the millennial-scale climate changes are under discussion (e.g., Broecker et al., 1989; Condron and Winsor, 2012; Carlson et al., 2007; Murton et al., 2010; Tarasov and Peltier, 2005).

Broecker et al. (1989) suggested that the freshwater of the Lake Agassiz was discharged via the St. Laurence River at the onset of the YD period. Later, the Arctic route via the Mackenzie River from the Lake Agassiz was suggested based on the geological evidence of the vast erosion of the Mackenzie River at the onset of YD period (Murton et al., 2010). An ocean model indicated that the meltwater discharged from St Laurence River flows southward in the Atlantic and does not lower the salinity of the NADW formation areas, but the freshwater discharged to the Arctic Ocean effectively lowers the salinity enough to damp the NADW formation (Murton et al., 2010). Very recently, the salinity drop in

the western Arctic at the offshore of the Mackenzie delta at the onset of the YD period was indicated by the negative $\delta^{18}O$ excursion of planktic foraminifera in sediment cores from the Makenzie delta area (Fig. 1-4; Keigwin et al., 2018). This finding supports the idea that the meltwater discharge to the western Arctic damped the AMOC at the onset of the YD period.

The data of Keigwin et al. (2018) indicated that freshwater discharge continued during the NA period (14.5-12.9 ka) before the YD period, though the degree of negative excursion of $\delta^{18}O$ was smaller than that at the onset of the YD period (Fig. 1-4) Sedimentation rate at the Mackenzie Delta between 12.9 and 14.5 ka was extremely high (>1000 cm/kyr) in the Mackenzie delta (Fig. 1-4; Keigwin et al., 2018). This also suggests that intense river discharge continued during the BA period. However, the AMOC did not weaken during the BA period (Fig. 1-5; Ritz et al., 2013). This disagreement suggests that the response of the AMOC to freshwater input was not simple. Potential factors affecting the response is the route and amount of meltwater from the Laurentide ice sheet, as suggested by Murton et al. (2010). Thus, the identification of route of freshwater discharge from the Laurentide Ice Sheet to the Arctic Ocean during the BA period is important to understand the relationship between freshwater discharge and the AMOC.

The relative amounts of meltwater discharged from the Laurentide ice sheet at the

onset of the Younger Dryas period were estimated to be 50 % to the Gulf of Mexico via the Mississippi River, 30% to the western North Atlantic via St. Lawrence River, and 20% to the Arctic Ocean via the Mackenzie River by an ice sheet model (Tarasov and Peltier, 2005). However, there is poor geological evidence other than the excursion of planktonic foraminifera (PF) $\delta^{18}O$ in the Gulf of Mexico sediment cores (Williams et al., 2012). The quantitative estimation of meltwater to different ocean basins is thus indispensable to discuss the role of freshwater discharge in the AMOC.

In this study, I refined the stratigraphy of western Arctic Ocean sediments and discussed the sediment provenances and sedimentation processes of event layers during the last glacial period. A new empirical calibration method was developed to more accurately determine the sediment age of the carbonate-lean sediments in the western Arctic Ocean. Based on the established stratigraphy with age controls, I calculated the amount of meltwater which flowed from the Laurentide ice sheet into the Arctic Ocean during the BA period and discussed the relationship between the AMOC and the freshwater inflow to the Arctic Ocean during the BA period.

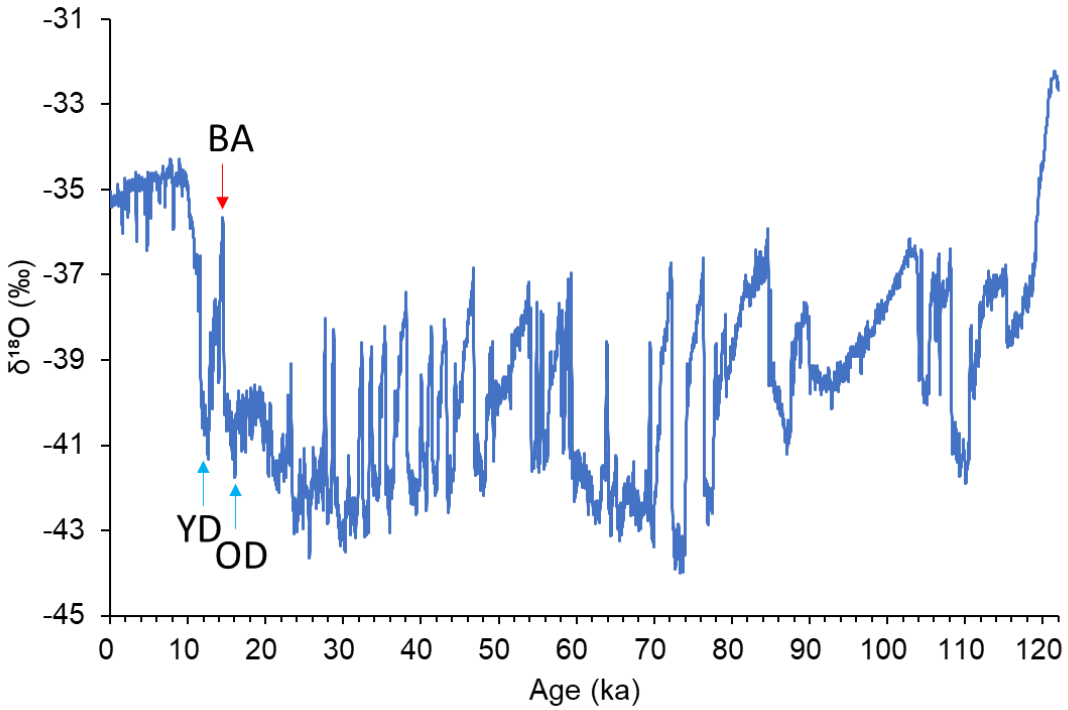

Fig. 1-1. Changes of the ice water $\delta^{18}O$ in Greenland ice cores (NGRIP, GRIP and GISP2; Data form Seierstad et al., 2014). YD: Younger Dryas, BA Bølling-Allerød, OD: Older Dryas.

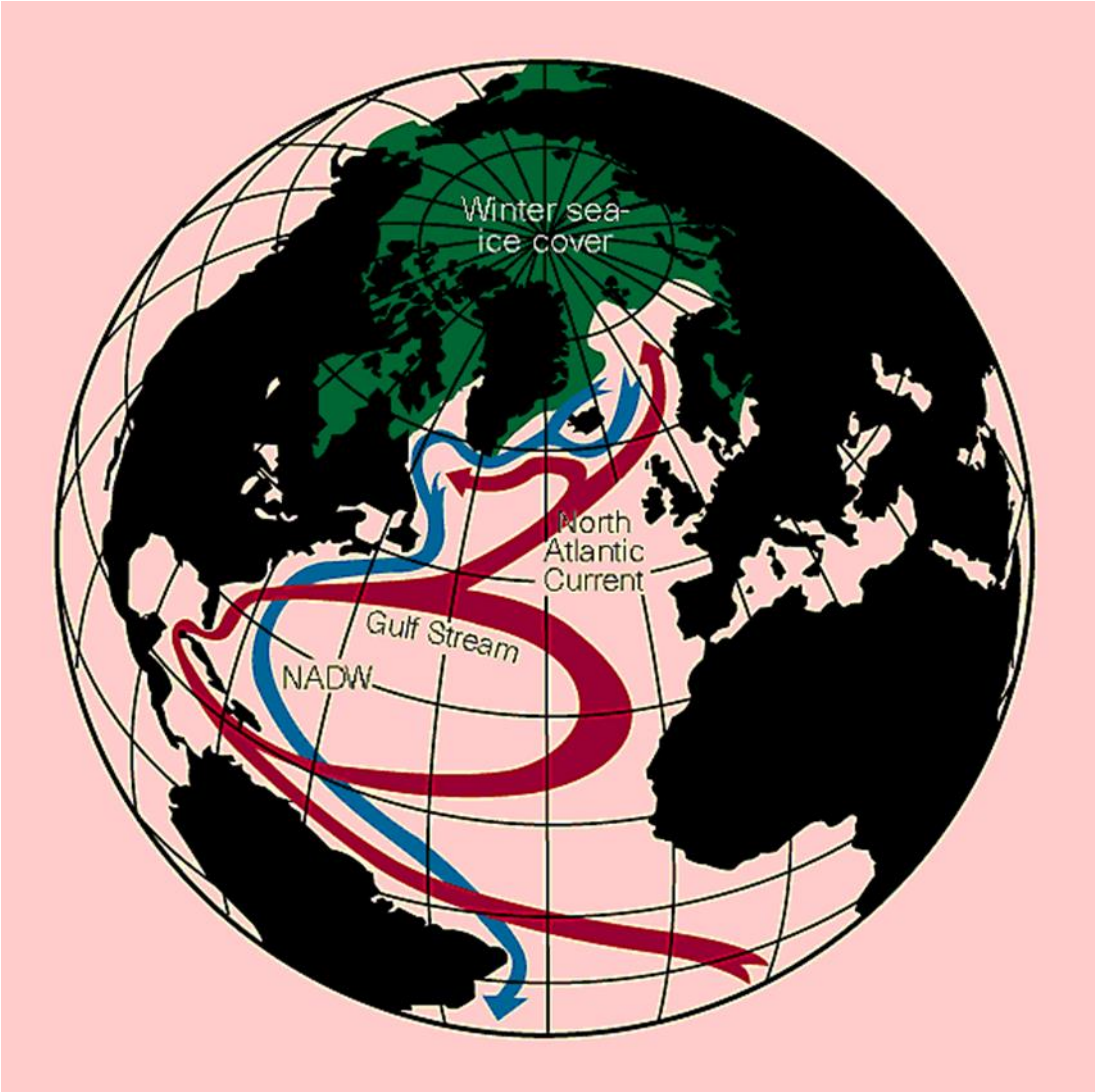

Fig. 1-2. Simplified cartoon of the Atlantic meridional overturning circulation (Rahmstorf, 1997). Arrows indicate warmer surface currents (red) and cold North Atlantic Deep Water (NADW; blue).

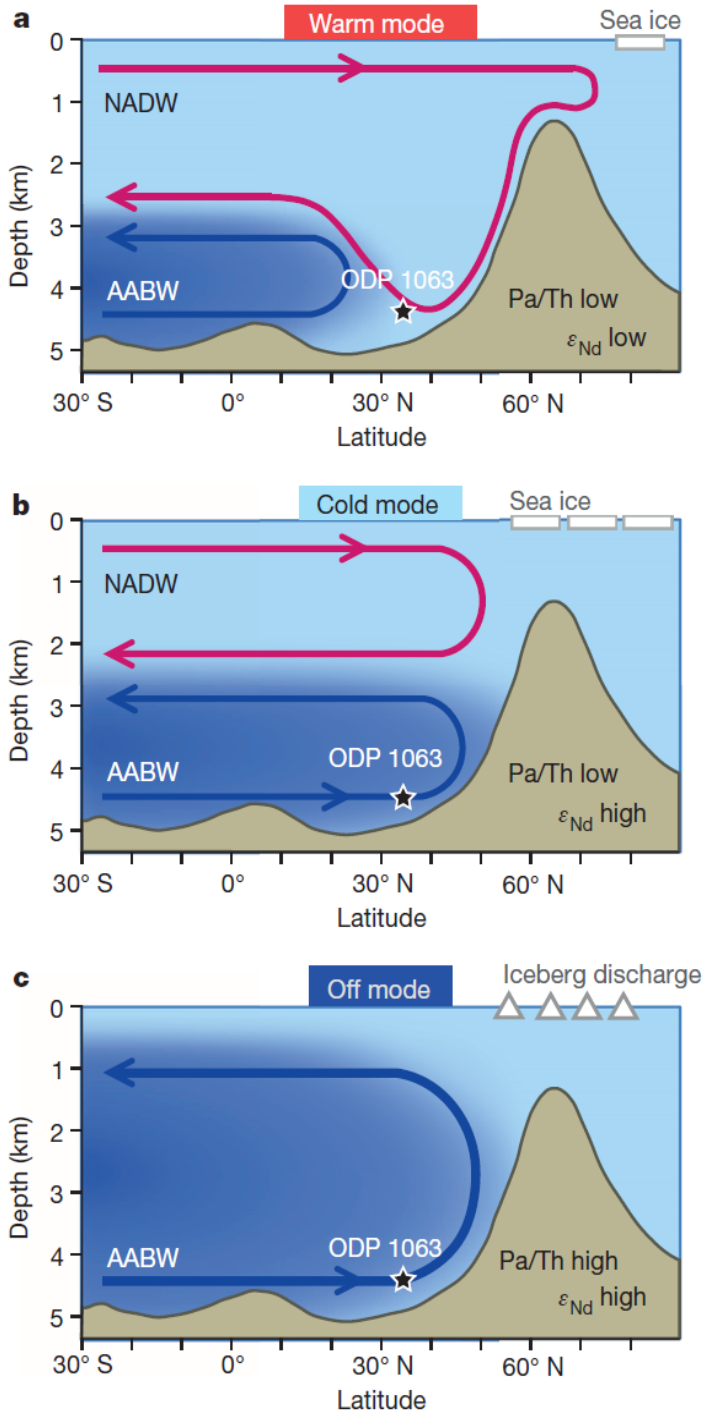

Fig. 1-3. Concept model of warm, cold and off modes of the Atlantic meridional overturning circulation (Böhm et al., 2015). NADW: North Atlantic Deep Water, AABW: Antarctic Bottom Water.

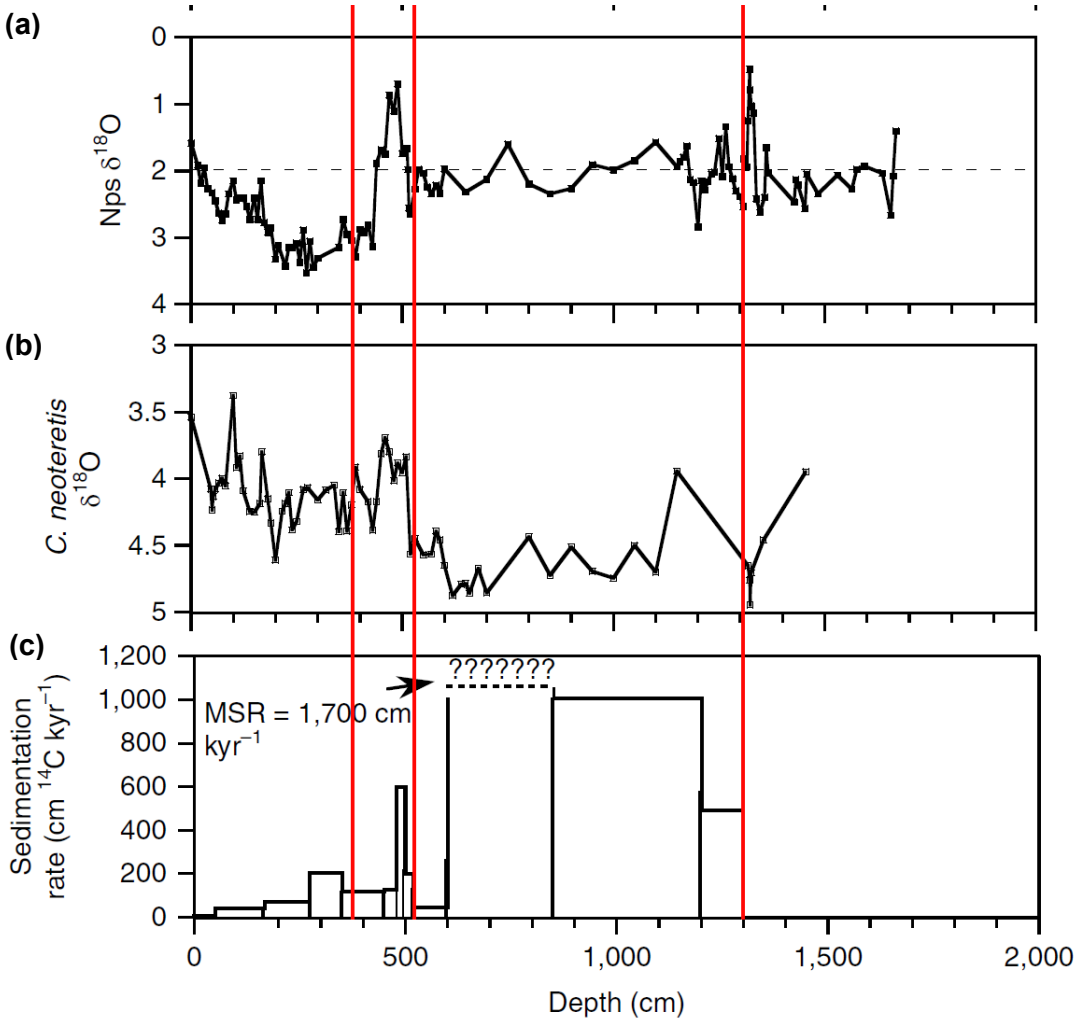

Fig. 1-4. $\delta^{18}O_{Nps}$ (a), the *C. neoteretis* (benthic) $\delta^{18}O$ (b) and sedimentary rate (c) of JPC-15/27 core in the eastern Beaufort Sea (Keigwin et al., 2018). $\delta^{18}O_{Nps}$ is low at early in the BA period at 14.6 ka (red line at 1,300 cm) and during the YD (11.7–12.9 ka) (red lines at ~380 and 510 cm).

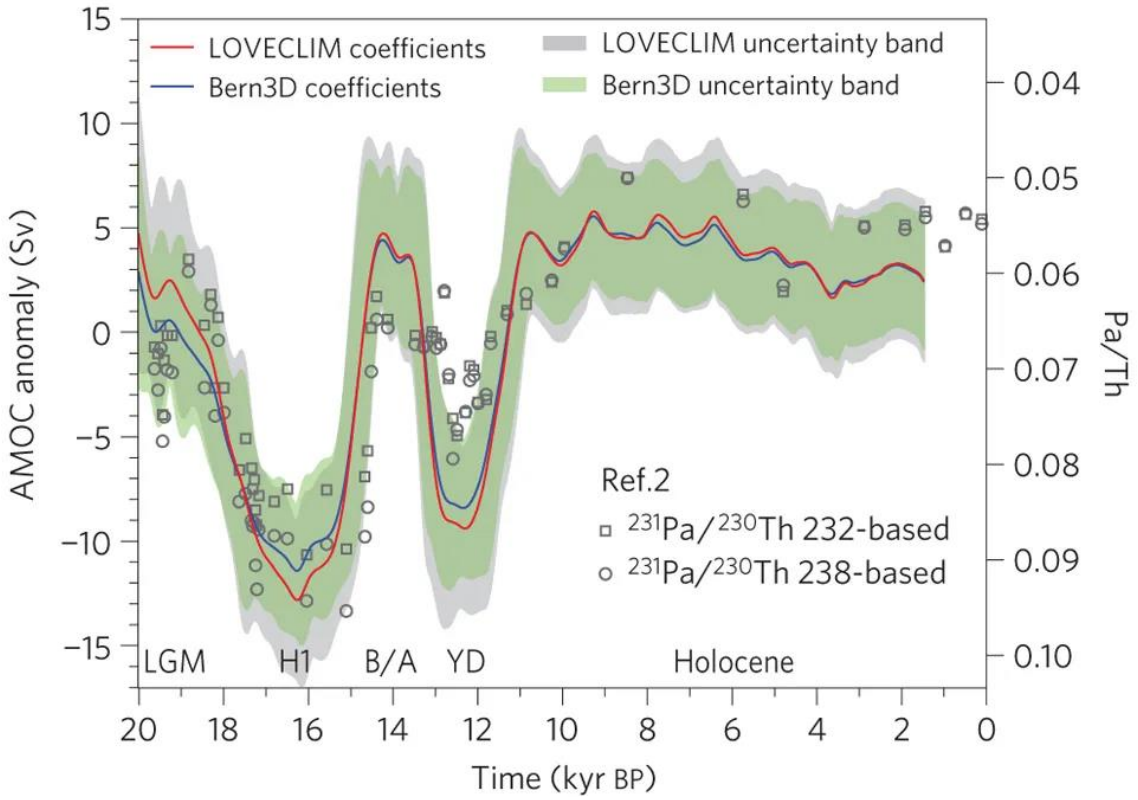

Fig. 1-5. Variability of AMOC anomaly based on changes in $^{231}Pa/^{230}Th$ ratio during the last 20 kyr (Ritz et al., 2013).

CHAPTER II.
Development of Age Estimation Method using the Ramped Pyrolysis ^{14}C Dating

2.1. Introduction

Robust stratigraphic age constraint is key for the generation of paleoclimate records. Biogenic carbonate radiocarbon (^{14}C) is commonly used for dating geological material to ~50 ka old. However, ^{14}C dating is difficult to apply to sediments that lack sufficient amounts of in situ biogenic $CaCO_3$. In such sediments, ^{14}C dating resorts to bulk organic matter (OM) (Andrews et al., 1999; McGeehin et al., 2001; Park et al., 2017). However, the bulk OM produces ^{14}C ages older than in situ material in certain systems, because they generally contain old allochthonous carbon (Andrews et al., 1999, McGeehin et al., 2001). For example, the ^{14}C ages of suspended or deposited bulk OM in the surface waters of the Arctic Ocean and in the surface sediments of the Siberian river estuaries were ~500 to 4,000 yr BP and ~600 to 13,000 yr BP old, respectively, reflecting the contribution of old allochthonous carbon (Benner et al., 2004; Guo et al., 2004). Bulk OM ^{14}C ages in sediment core tops are often used as a presumably constant offset correction for downcore sediment ages, assuming constant supply of old, allochthonous carbon, constant reservoir age, and constant bioturbation depths and rates. However, none of these factors is likely to be really constant, leading to potential inaccuracies in age estimation despite high analytical precision of dating. An alternative approach is the measurement of ^{14}C ages of the marine-sourced organic compounds (Eglinton et al., 1996), but this method is time

and effort consuming, and the collection of satisfactory amounts of these compounds for ^{14}C measurement is not guaranteed in all cases.

A recently developed method of ramped pyrolysis (RP) ^{14}C dating of bulk OM was successfully applied to carbonate-poor Holocene sediments from the Antarctic margin (Rosenheim et al., 2008, 2013; Subt et al., 2016, 2017). This approach is based on the notion that young, autochthonous OM is pyrolyzed at lower temperatures than older, allochthonous OM, so that ^{14}C ages of low-temperature carbon fractions are closer to the age of in situ material, although still with some offsets. To get further insights into the application of this method and to extend it geographically and stratigraphically, we applied the RP ^{14}C dating of bulk OM into postglacial sediments from the Alaskan margin, western Arctic Ocean (Fig. 2-1). This area represents a high-latitude glacimarine environment, similar to the Antarctic margin with respect to the low in situ organic production and high contribution of old, terrigenous organic carbon (e.g., Domack et al, 1999; Stein, 2008). In this study we capitalize on the independent age constraints for the analyzed sediments developed in prior studies on the same or correlative cores (Darby et al., 2009a; Lisé -Pronovost et al., 2009; Keigwin et al., 2018). A comparison of these ages with the RP ^{14}C data enabled us to develop a new, empirical method of determining the actual age of sediment from the pyrolyzed organic components.

2.2. Material and methods

2.2.1. Sediment material

Two piston sediment cores, HLY0501-JPC5 (1628 cm long; 72°41.7'N, 157°31.2'W; 415 m water depth) and -JPC6 (1554 cm; 72°30.7'N, 157°02.1'W; 673 mwd), were collected from the NW Alaskan margin in the western Arctic Ocean during the 2005 Healy-Oden Trans Arctic Expedition (Fig. 2-1; HOTRAX'05; Darby et al., 2009a). Since piston cores lose the core top sediment, trigger cores TC5 and TC6 were used to supplement the upper stratigraphy in composite records, with the JPC5 and JPC6 adjusted by +75 cm (Darby et al., 2009b) and +147 cm (Ortiz et al., 2009), respectively.

Several studies dealt with various stratigraphic, lithological, and paleoclimatic aspects of these records (e.g., McKay et al., 2008; Darby et al., 2009b; Lisé-Pronovost et al., 2009; Polyak et al., 2009, 2016). Both cores can be principally divided into two lithostratigraphic units (Fig. 2-2): the Holocene olive-grey, fine-grained, bioturbated marine mud (upper 1300 cm composite core depth in JPC/TC5, and 1000 cm in JPC/TC6), and the underlying grey muds with variable coarse ice-rafted debris (IRD) and indistinct laminations, attributed mostly to iceberg/meltwater dominated glacial/deglacial environments (McKay et al., 2008; Polyak et al., 2009). Non-stratified, fine-grained sediments at the bottom of JPC5 and in the lower part of JPC6 were tentatively attributed

to deposition under solid pack ice or ice shelf during the Last Glacial Maximum (LGM) (Fig. 2-2; Polyak et al., 2009; Zhang et al., 2019).

Organic matter was analyzed in several studies on core JPC5 (McKay et al., 2008; Faux et al., 2011; Polyak et al., 2016). In the Holocene section total organic carbon is relatively high for Arctic sediments, gradually increasing up-core to ~1.5 %. An accompanying decrease in C/N and $\delta^{13}C$ values indicates a progressive rise in the marine OM component. Biomarkers, such as sterols and tetraethers, further corroborate the mostly marine composition of the Holocene sediments, although with a consistent contribution from terrestrial sources (Faux et al., 2011; Polyak et al., 2016). The deglacial sediments have overall lower TOC and higher C/N and $\delta^{13}C$ values, as well as branched tetraether content, all indicating considerably higher terrestrial inputs (McKay et al., 2008; Polyak et al., 2016).

Age controls for the Holocene section included six ^{14}C measurements on mollusk shells from core JPC5 (Table 2-1a; Darby et al., 2009b) and several paleomagnetic tie points in core JPC6 (Table 2-1b; Lisé-Pronovost et al., 2009). The age framework for the glacial section was tentatively based on correlation to longer stratigraphies from the western Arctic Ocean (Polyak et al., 2009; Zhang et al., 2019).

In this study, five samples from each core were collected for the RP ^{14}C dating from

both the Holocene and glacial sections at 112, 955.5, 1155, 1295 and 1632 cm composite depth in JPC/TC5 (Table 2-2), and 157, 957, 1077, 1377 and 1688 cm in JPC/TC6 (Fig. 2-2). The initial age model for the Holocene samples was adopted from prior data, where two new samples in JPC5 were taken from the same core levels with previously dated mollusk shells (Table 2-1), and others were estimated by inter/extrapolation from ^{14}C and/or paleomagnetic-based ages (Tables 2-1). The age tie points for the glacial section were derived by correlation to core JPC15/27 from the Mackenzie River delta area further east (Fig. 2-1), dated by ^{14}C on tests of the planktic foraminifera *Neogloboquadrina pachyderma* (sinistral) (Nps) (Tables 2-2; Keigwin et al., 2018). The correlation was aided by dolomite-rich IRD layers, expressed as dolomite/quartz ratio (Fig. 2-2) (Yamamoto et al., 2017). These layers have been related to pulsed iceberg discharges from the Laurentide Ice Sheet eroding dolomitic rocks in the Canadian Arctic (Bischof et al., 1996; Polyak et al., 2009; Stokes et al., 2005). Major dolomitic peaks in the deglacial section of JPC5 and JPC6 were correlated to meltwater (MW) events identified in JPC17/25 and dated to 12.9 ka and 14.5 ka (Keigwin et al., 2018) (Fig. 2-2). By means of this correlation, three ^{14}C-dated tie point were spliced directly to the RP samples (Tables 2-2).

Local reservoir correction (ΔR) for ^{14}C calibration differed between the used data sets due to origin of dated biogenic carbonates from different hydrographic environments

(Darby et al., 2009b; Keigwin et al., 2018). Thus, no ΔR was applied to datings on molluscs in JPC5 as they live in young Atlantic-originating intermediate waters (Darby et al., 2009b). Similarly, no ΔR was used for foraminifers from JPC17/25 except for 200-yr ΔR applied to deglacial Younger Dryas samples (Keigwin et al., 2018). ΔR of ~480 years was well substantiated for Holocene sediments from the Chukchi Sea shelf bathed by surface waters with a strong Pacific component (Pearce et al., 2017).

2.2.2. Ramped pyrolysis ^{14}C dating

Freeze-dried sample was acidified in 1 N HCl for four hours with occasional stirring until no bubbles occurred indicating removal of carbonates. Thereafter, the sediment was rinsed with pure water until reached the pH = 7. The rinsed sample was dried in a dryer at 50 °C and pulverized using a mortar and pestle. The sample was placed in a quartz reaction tube (baked at 900 °C; for 4 hours) packed with 0.5—1 g quartz wool (baked at 525 °C, 2 hours) and quartz wool was placed thereon. The tube was set in a combustion chamber, ultra-high purity (UHP) He was flowed through the quartz reaction tube at 34 mL/min, and mixed O_2 (4 mL/min) and He gas (7 mL/min) mixed in downstream of the sample through the annular space between the reactors (Rosenheim et al., 2008). Pyrolysis was performed from room temperature to 900 °C at a heating rate of 5 °C /min.

The pyrolysates were oxidized to CO_2 downstream of the confluence of the oxygenated gas stream with the stronger He flow on copper oxide, nickel, and platinum wires at constant 800 °C. Carbon dioxide was trapped in a 9-loop, thin glass trap, partially submerged in liquid N_2 and partially in air at room temperature (to melt any CO2 "snow" and refreeze in the next loop), and then purified in a vacuum line using liquid nitrogen and isopropanol kept at the solid-liquid phase transition with liquid nitrogen. Ultimately, the samples were quantified using a capacitive diaphragm manometer, transferred to a Pyrex tube with CuO and Ag wire (all pre-baked at 525 °C, 2 hours), and sealed. Generated CO_2 splits were collected every 20 μg and were sequentially numbers splits 1-6. The collected CO_2 was recombusted at 525 °C for 2.5 hours in a to ensure that every sample had been raised to such a temperature to minimize the chance of sulfur oxides to poison the graphitization process. Recombusted CO_2 was purified and graphitized in a vacuum line. Measurements of $\Delta^{14}C$ were performed with the National Electrostatics Corporation Carbon Accelerator Mass Spectrometry (AMS) of University Museum, the University of Tokyo. To collect enough amounts of CO_2 with smaller temperature range, we repeated pyrolysis for the sample of JPC5 880.5 cm over a higher resolution of 9 temperature intervals (S1-S9).

Generated conventional ^{14}C ages were converted to calendar ages using the CALIB7.04

program and Marine13 dataset (Reimer et al., 2013). Local reservoir correction (ΔR) was taken as 477±60 years according to Pearce et al. (2017).

2.3. Results

Pyrograms indicate that degradation of organic matter started from 100—160 °C and ended around 600°C in all samples (Fig. 2-3A, B), showing a bi- to trimodal distribution with the minor peak at 280 to 330 °C (average 300 °C) and two main peaks (shoulders) at 390─420 °C (average 400 °C) and 510─560 °C (average 540 °C) (Fig. 2-2A, B). The amount of pCO_2 decreased by half at about 50 °C from the peaks on both the low and high temperature sides (Fig. 2-2A, 2-3A, B). The CO_2 amount of these three peaks was quantified as the G1, G2 and G3 components by assuming that the peaks have a Gaussian (G) distributions centered at 300, 400 and 540 °C, respectively, and the peak width of 50 °C (Fig. 2-3C). The relative abundance of the G1 component was the lowest in all samples and decreased with increasing core depth (Fig. 2-4). The abundance of the G2 component had the opposite pattern with the highest values in all samples, increasing with depth (Fig. 2-4). The G3 component was largely unchanged with depth (Fig. 2-4).

The $\Delta^{14}C$ values decreased, and the ^{14}C ages increased accordingly from the low to high temperature splits in the same samples and with the core depth between the samples

(Fig. 2-5). Some In the oldest samples ^{14}C ages were not calculated accurately for because of $\Delta^{14}C$ values drip from below the detection or quantification limit. The first four splits, predominated by the G1 component, have an almost identical $\Delta^{14}C$, as exemplified by the JPC5 955.5-cm sample (Fig. 2-2C). The ^{14}C ages of split 1 were ~2 to 7 kyr older than the initial ages (Tables 2-1, 2-2 and 2-5). The age difference increased downcore to especially large values in samples from the deglacial sediment (Fig. 2-5).

The bulk pyrolyzed OM $\Delta^{14}C$ values ($\Delta^{14}C_{cb}$) were calculated using the following equation:

$$\Delta^{14}C_{cb} = \frac{\sum_i^n \Delta^{14}C_i \times m_i}{\sum_i^n m_i},$$

where the subscript *cb* refers to calculated bulk OM $\Delta^{14}C$, m is the molar amount of CO_2 measured in each split, and $\Delta^{14}C_i$ is the measured radiocarbon content of each split (Table 2-3; Fig. 2-5C, D).

The $\Delta^{14}C$ values of G1, G2 and G3 components were calculated as:

$$\Delta^{14}C_{\text{split n}} = \alpha_n(\Delta^{14}C\ G1) + \beta_n(\Delta^{14}C\ G2) + \gamma_n(\Delta^{14}C\ G3),$$

where α_n, β_n and γ_n are the fractions of G1, G2 and G3 components of split n. The $\Delta^{14}C$ values of G1, G2 and G3 components were obtained for all samples by solving these simultaneous equations, and converted to ^{14}C ages (Figs. 2-6, 2-7). The resultant $\Delta^{14}C$ values consistently decrease between the components from G1 to G3 and between the samples with the core depth (Fig. 2-6A, B). G1-G3 of from the lowermost samples (1632 cm of in core JPC5 core and 1638 cm of in JPC6) core are not used for discussion because they use due to quantitative or detection limit very low $\Delta^{14}C$ values in the calculations.

2.4. Discussion

2.4.1. The origin of the G1, G2 and G3 components and their age interpretation

The sedimentary organic matter contains a mixture of contemporary and older carbon that has been through cycles of diagenesis, erosion, and redeposition (e.g., French et al., 2018). During the pyrolysis experiments, the degradation of functional groups and moieties yields volatile pyrolysates according to the thermal stability of their structures (Durand, 1980; Williams et al., 2014; Hemingway et al., 2019). Bioavailable compounds are decomposed at low temperatures, whereas condensed molecules are not easily degraded (Hatcher et al., 1983; Burdige, 2007). Durand (1980) showed that during the heating (4 °C /min.) of immature sedimentary kerogen, its oxygen content decreases at

the first stage (25 to 350—450 °C), the hydrogen content decreases next (350 to 500 °C), and the aromatic structures decrease at temperatures >500 °C. Williams et al. (2014) reported that cellulose was degraded at 300—400 °C, humic acid at 400—600 °C, and lignin at >600 °C during the heating of mixtures of organic matter at 5 °C/min (Fig. 2-3A). Williams et al. (2014) suggested that glycosidic bonds (carboxyl and carbonyl groups and esters) are broken first, followed by aliphatic structures, and finally aromatic structures at the highest temperatures. Hemingway et al. (2019) further suggested that the bonding of organic molecules with mineral surface enhances the preservation of organic molecules in the water and sediments, based on the relationship between the activation energy of degradation and the radiocarbon age of dissolved riverine organic matter (DOM) as well as soil and marine sediment OM.

The order of thermal stability outlined above is consistent with the pattern of increase in radiocarbon ages in ramped pyrolysis experiments, which generally yield younger carbon at lower temperatures (Rosenheim et al., 2008; 2013; Subt et al., 2016; 2017; Hemingway et al 2019). One interpretation of this pattern is based on the notion that in the mixture of marine and terrestrial organic matter, the latter is generally older than the OM produced in marine environments (Pearson et al., 2001; Rosenheim et al., 2008; 2018). Hemingway et al. (2019), however, showed that the pyrolysis of terrestrial soil

OM and DOM also yields younger carbon at lower temperatures. This result suggests that more mechanisms are needed to explain the observed ^{14}C age increase. For example, during diagenesis, OM loses oxygen functional groups and aliphatic structures and condenses to form aromatic structures (e.g., Tissot and Welte, 1978). The condensation process likely stabilizes older OM, so that more condensed and aged OM yields older carbon at higher temperatures. In addition, the OM attached to mineral surface is protected against microbial degradation and, thus, retains older carbon until it is pyrolyzed at higher temperatures (Hemingway et al., 2019). Although the exact mechanism is still not well understood, a close relationship between the chemical stability and age of sedimentary organic matter appears to be robust.

While the correspondence of the obtained G1-G3 components to chemical structures of the OM is still largely speculative, their distribution pattern is consistent with the results discussed above. We infer that these components are successively derived from the degradation of glycosidic bonds (G1), aliphatic structures (G2), and aromatic structures (G3). The ^{14}C data of the G1 component are the closest to the model ages, but with some offsets that appear to increase in deglacial sediments (Fig. 2-5). This pattern suggests that mostly marine OM-originating G1 contains an admixture of terrestrial material that may be higher in glacially mediated environments. The downcore increase

in the contents of G3 and especially G2 components probably reflects elevated contribution of terrestrial and/or overall older OM types, which contain more aliphatic and aromatic moieties (e.g., Tissot and Welte, 1978). This pattern is consistent with the distribution of TOC, C/N, $\delta^{13}C$, and biomarkers in core JPC5, all indicating an increase in the terrestrial component downcore, especially in the deglacial sediments (McKay et al., 2008; Faux et al., 2011; Polyak et al., 2016). The difference in the distribution pattern of the G2 and G3 components (Fig.2- 4) is not easily understood and requires more detailed investigation. We note also that our interpretation does not account for all of the potential complexities, in particular, the role of the adsorption of OM on mineral surfaces in retaining OM during the pyrolysis (Hemingway et al., 2019).

2.4.2. Age estimates from RP ^{14}C data

A constant offset value for old carbon contamination is commonly used to determine sediment ages from bulk OM ^{14}C dating (e.g., Andrews et al., 1999; McGeehin et al., 2001; Park et al., 2017). However, our results demonstrate that the offsets between pyrolysate ^{14}C ages are not constant and increase with sediment depth to especially large offsets values in samples from the deglacial sediments (Fig. 2-5). This larger difference is likely caused by a higher contribution of terrigenous organic matter, as discussed above

in glacial/deglacial environments, consistent with a high branched and isoprenoid tetraether (BIT) index measured in these sediments in JPC5 (Polyak et al., 2016).

As the relationship of pyrolysis temperature with the age difference between the G1 to G3 components is appears to be very robust in each sample (Fig. 2-7), we infer that it can be used to determine the offset between the projected actual sediment age. For this purpose, to estimate the sediment age offset for the G1 component, we used two empirical relationships, one based on the slope of RP ^{14}C ages to pyrolysis temperature (S) (Method 1; Fig. 2-8A):

Offset Projected age = G1-(115.4S – 2.3482), $R^2 = 0.97$ (Eq. 1),

and another based on the age difference between the G1 and G3 components (Method 2; Fig. 2-8B):

Offset Projected age = G1-(0.4776 (G3-G1) – 2.3958), $R^2 = 0.96$ (Eq. 2).

A comparison of the two estimation methods shows that they produce very similar results (Table 2-5 Figs. 2-8, 2-9). As the second equation based on the G3-G1 difference is

simpler, this method makes for an easier age estimation tool. When compared to the independent initial ages, both methods result in only small offsets for the Holocene sediments, under 200 and 400 years for conventional and calendar ages, respectively (Table 2-5 Figs. 2-8, 2-9). In deglacial sediments offsets are larger and constitute up to 700/800 years in JPC6 and 1,100/1,200 years in JPC5 for conventional and calendar ages, respectively. These larger offsets may result from a number of factors, such as the prevalent terrestrial OM and uncertainties with ΔR and with the initial age controls obtained by means of correlation (Fig. 2-2).

Overall, these results suggest that our new, simple method of estimating the sediment ages from the RP ^{14}C measurements on bulk OM is well applicable to Arctic Ocean sediments with prevailing marine OM composition, primarily in the Holocene in the postglacial age range, ~15 ka. The application of this method to older sediments formed in glaciogenic environments may be complicated by the diminished amounts of young marine OM, as indicated by larger offsets between the RP-based and independent age constraints (Fig. 2-8). In the oldest glacial/deglacial samples the derived $\Delta^{14}C$ values are below the detection or quantification limits (Table2-4). These low amounts which can result from a very low supply under glacial conditions and/or diagenetic transformations.

2.5. Conclusions

RP ^{14}C dating of bulk organic matter from postglacial Arctic Ocean sediments yielded volatile carbon grading from younger to older ages with increasing pyrolysis temperatures. We use the relationships between the ages of different pyrolysate components and the pyrolysis temperature to propose a new, simple method of estimating sediment ages based on the RP ^{14}C data. Ages derived by this method are reasonably close to the independent age controls, including those generated on biogenic carbonates, with offsets mostly within 700 years. The offset for calibrated ages is considerably higher, up to 1,700 years, which may be related to an additional uncertainty with the reservoir ages. The $\Delta^{14}C$ values from the oldest samples were below the detection or quantification limits. Overall, the proposed RP-based ^{14}C age estimation method has a potential for application to sediments impoverished in biogenic/authigenic carbonates and with relatively low amounts of marine organic matter. More research is needed to verify this approach to other marine regions with similar depositional environments, such as the Southern Ocean, and to comprehend the underlying processes of the OM burial and transformation.

Table 2-1. The initial age constraints for cores JPC5 and JPC6.

HLY0501-JPC5

Adjusted depth (cm)	Initial ages (yr BP)		Material	References
	Conventional	Calendar		
112	1,930	1,001	Bivalve shells	Darby et al., 2009b
559	4,465	4,006		
644.5	4,820	4,510		
764.5	5,220	5,007		
875	5,885	5,804		
955.5	6,395	6,343		
1353	11,100	12,415	Planktic foraminifera	Keigwin et al., 2018 (by correlation of MW event)

HLY0501-JPC6

Adjusted depth (cm)	Initial ages (yr BP)		Material	References
	Conventional	Calendar		
211	—	2,030	Paleomagnetic correlation with age-constrained records	Lisé-Pronovost et al., 2009
259	—	2,150		
375	—	3,580		
653	—	5,780		
662	—	5,680		
674	—	6,000		
733	—	6,330		
886	—	7,800		
926	—	7,680		
949	—	7,830		
1017	11,100	12,415	Planktic foraminifera	Keigwin et al., 2018 (by correlation of MW events)
1357	12,800	14,124		

Table 2-2. The inital ages for the RP samples from core JPC5 and JPC6.

HLY0501

Core	Adjusted depth (cm)	Initial ages (conv. yr BP)	Initial ages (cal. Yr BP)	Age constraints
JPC5	112	1,930	1,001	^{14}C dating of bivalve shell (Darby et al., 2009b)
	955.5	6,395	6,343	^{14}C dating of bivalve shell (Darby et al., 2009b)
	1155	7,500	7,600	Extrapolation from ^{14}C ages of bivalve shell (Darby et al., 2009b)
	1295	—	—	
	1632	—	—	
JPC6	157	—	1,600	Extrapolation from paleomagnetic tie points (Lisé-Pronovost et al., 2009)
	957	—	9,700	Extrapolation from paleomagnetic tie points (Lisé-Pronovost et al., 2009)
	1077	11,800	13,200	Interpolation between MW events correlated from ^{14}C ages of planktic foraminifers in core JPC15/27 (Keigwin et al., 2018)
	1377	12,900	14,600	Extrapolation from MW event correlated from^{14}C ages of planktic foraminifers in core JPC15/27 (Keigwin et al., 2018)
	1688	—	—	

Table 2-3. The $\Delta^{14}C$ values and ^{14}C ages of the calculated bulk OM.

Core	Depth (cm)	$\Delta^{14}C_{cb}$ (‰)	$^{14}C_{cb}$ age (conv. yr BP)
HLY0501-JPC5	1155	-853	15,410
	1632	-994	41,143
HLY0501-JPC6	157	-579	6,958
	1688	-992	38,977

Table 2-4. The $\Delta^{14}C$ values and ^{14}C ages of the G1-G3 peaks.

Core	Depth (cm)	$\Delta^{14}C$ (‰)			^{14}C age (con. yr BP)		
		G1	G2	G3	G1	G2	G3
JPC5	112	-320	-528	-705	3,098	6,035	9,808
	955.5	-625	-780	-879	7,887	12,164	16,952
	1155	-679	-871	-924	9,137	16,472	20,653
	1295	-821	-954	-970	13,820	24,735	28,168
	1632	-962	-990	-999	26,269	36,993	55,490
JPC6	157	-354	-550	-684	3,510	6,414	9,254
	957	-769	-852	-943	11,771	15,347	23,012
	1077	-863	-943	-977	15,968	23,012	30,303
	1377	-897	-956	-985	18,259	25,092	33,736
	1688	-953	-994	-999	24,562	41,097	73,987

Table 2-5. Comparison of the initial model ages and the RP ^{14}C- ages obtained by the two estimation methods in cores JPC5 and JPC6. The plus marks indicate ^{14}C datings of mollusk shells; asterisks indicate ages correlated to MW events; other initial ages were estimated by inter/extrapolation (Table 2-2). Samples from JPC5 1632cm and JPC6 1688cm had Δ^{14}C values below the detection or quantification limits.

HLY0501-JPC5

Depth (cm)	Initial ages (Conv. yr BP)	Initial ages (Conv. yr BP)	RP ^{14}C-based ages (Conv. yr BP)	
			Method 1	Method 2
112	1,930	1,001	2,505	2,570
955.5	6,395	6,343	6,276	6,241
1155	7,500	7,600	6,668	6,327
1295	—	—	9,741	9,665

HLY0501-JPC6

Depth (cm)	Initial ages (Conv. yr BP)	Initial ages (Conv. yr BP)	RP ^{14}C-based ages (Conv. yr BP)	
			Method 1	Method 2
157	—	1,600	3,354	3,441
957	—	9,700	8,871	9,091
1077	11,800	13,200	11,690	11,819
1377	12,900	14,600	13,393	13,568

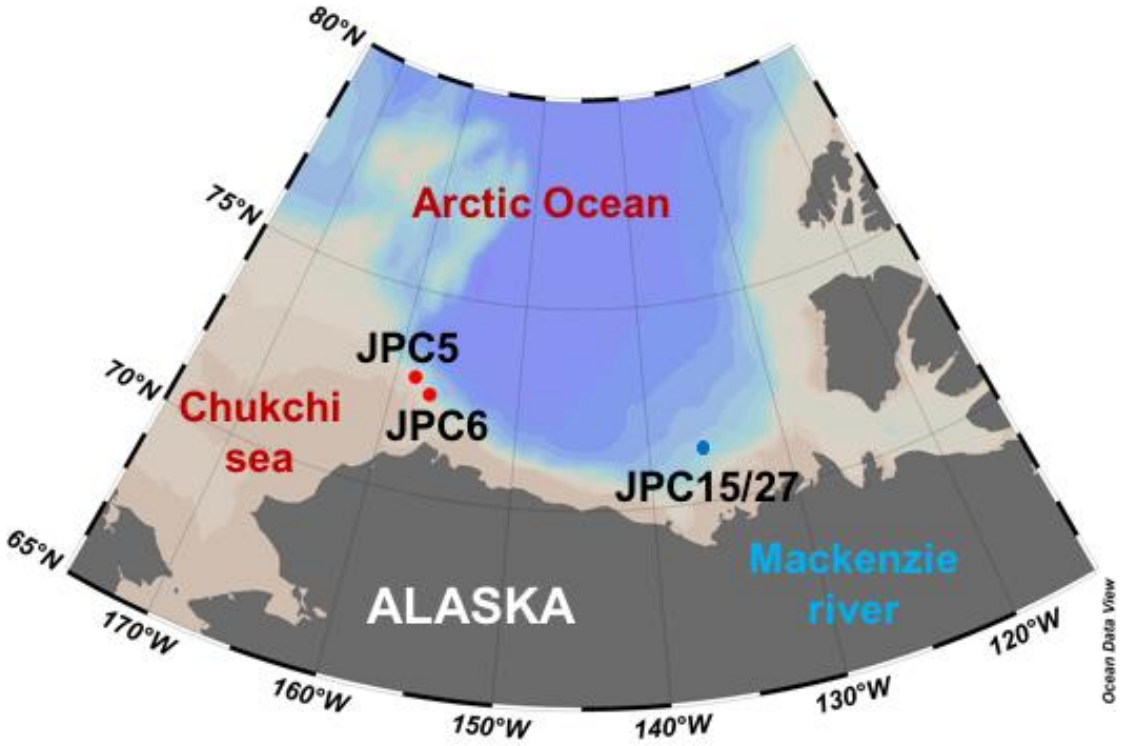

Fig. 2-1. Location of cores HLY0501 JPC5 and JPC6 (Darby et al., 2009a) and HLY1302 JPC15/27 (Keigwin et al., 2018).

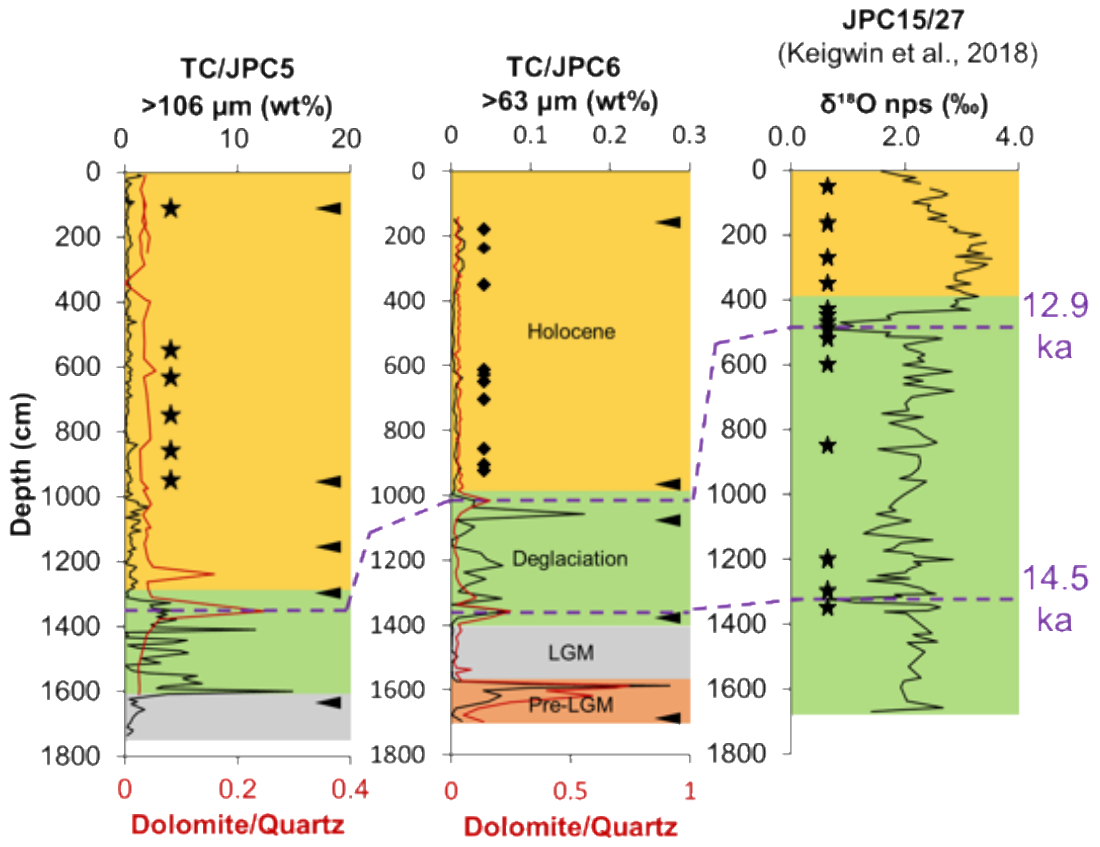

Fig. 2-2. Simplified stratigraphy for cores JPC5 and JPC6 (MacKay et al., 2008; Darby et al., 2009b; Polyak et al., 2009) and JPC15/27 (Keigwin et al., 2018). Lithostratigraphic units are color-coded: yellow – marine Holocene, green – deglacial, grey – glacial (LGM), brown – preglacial. Diagrams show the content of coarse grains (>106 µm in JPC5 (MacKay et al., 2008), >63 µm in JPC6 (Polyak et al., 2009, and new data)), dolomite/quartz ratio in JPC5 and JPC6 (from Yamamoto et al., 2017), and the Nps $\delta^{18}O$ in core JPC15/27 (Keigwin et al., 2018). The levels of ^{14}C ages on bivalves in JPC5 (Darby et al., 2009b) and planktic foraminifers in JPC15/27 (Keigwin et al., 2018) are marked by stars; paleomagnetic tie points in JPC6 are marked by diamonds (Lisé-Pronovost et al., 2009). Samples taken from JPC5 and JPC6 for the RP ^{14}C analysis are indicated by arrowheads. Dashed lines show correlation of the deglacial MW events dated in core JPC15/27.

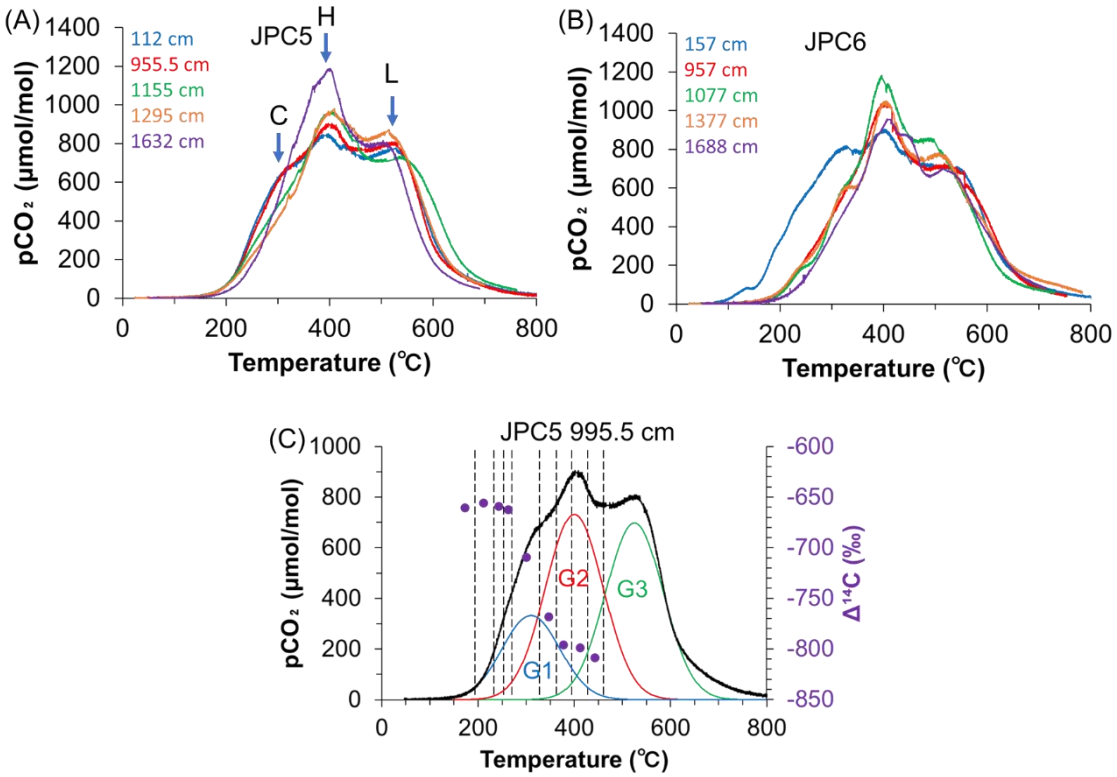

Fig. 2-3. Pyrograms for samples from cores JPC5 (A) and JPC6 (B). Three gaussian distribution peaks G1-G3 and the $\Delta^{14}C$ values of nine splits are shown for the sample from 955.5 cm in JPC5 (C). The dotted lines show upper and lower pyrolysis temperatures for all splits. C, H, and L in panel A indicate the pyrolysis temperature of cellulose, humid acid and lignin, respectively (Williams et al., 2014).

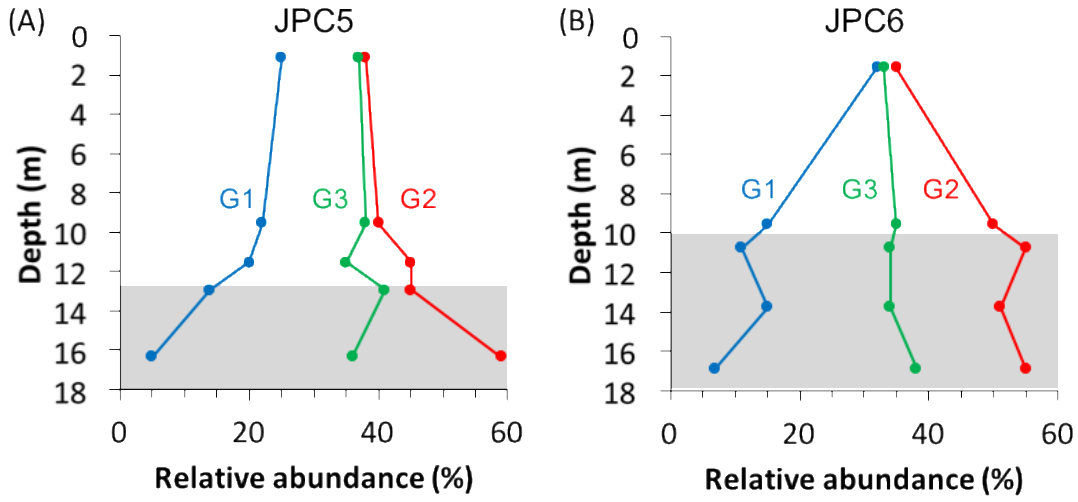

Fig. 2-4. The percentage of the gaussian component peaks G1-G3 in each sample from cores JPC5 (A) and JPC6 (B). Deglacial sediments are shaded.

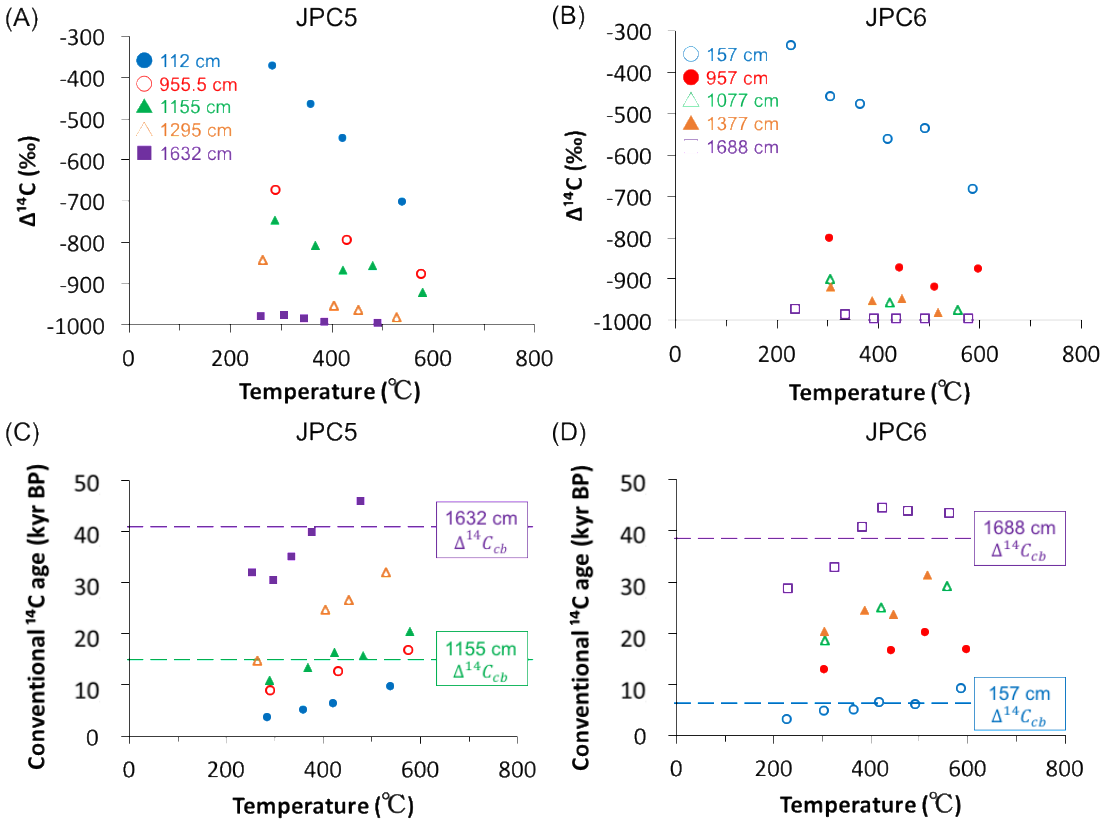

Fig. 2-5. The Δ¹⁴C values and conventional ^{14}C ages of splits in samples from cores JPC5 (A, C) and JPC6 (B, D), where all split ages were obtained. Dashed lines show ^{14}C ages of the calculated total organic carbon for samples at 1155 cm and 1632 cm in core JPC5 and at 157 cm and 1688 cm in core JPC6.

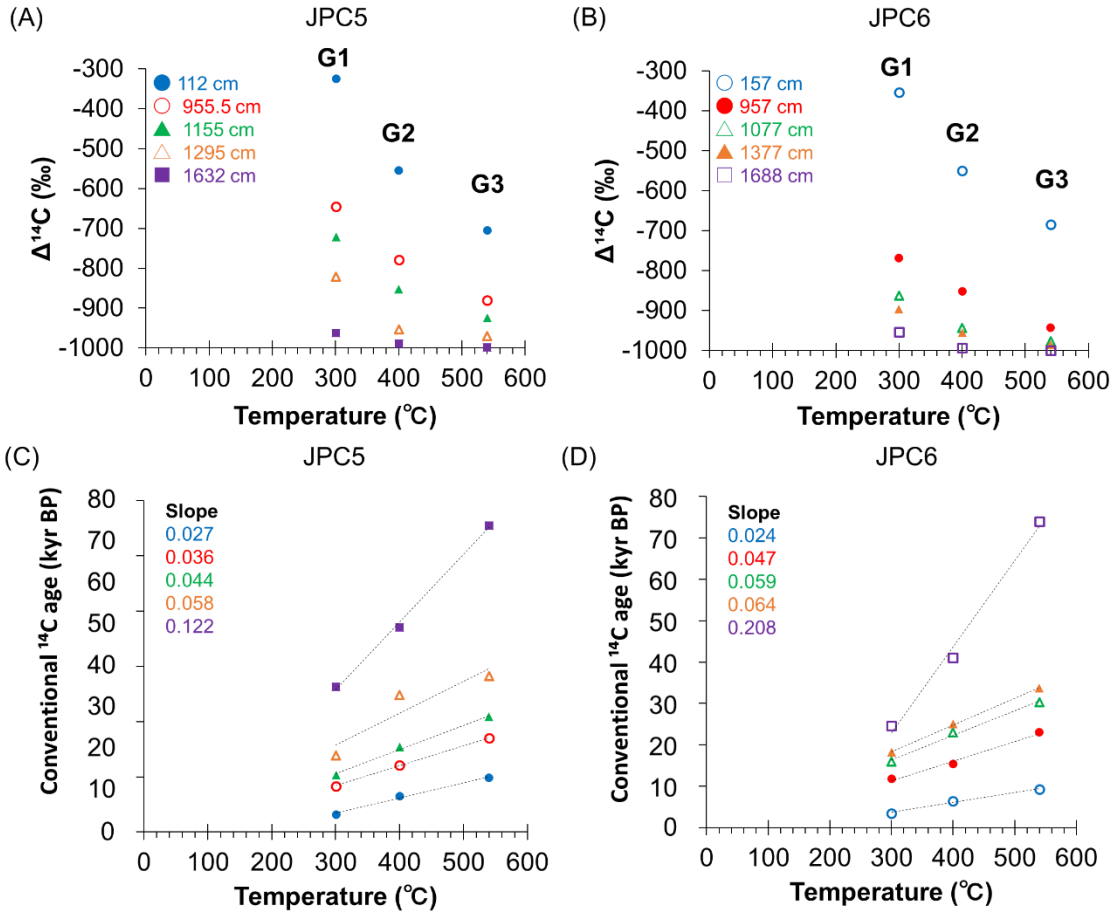

Fig.2- 6. Distribution of the $\Delta^{14}C$ values and conventional ^{14}C ages of the gaussian component peaks G1-G3 vs. pyrolysis temperature in cores JPC5 (A, C) and JPC6 (B, D). Slope values are indicated for ^{14}C ages.

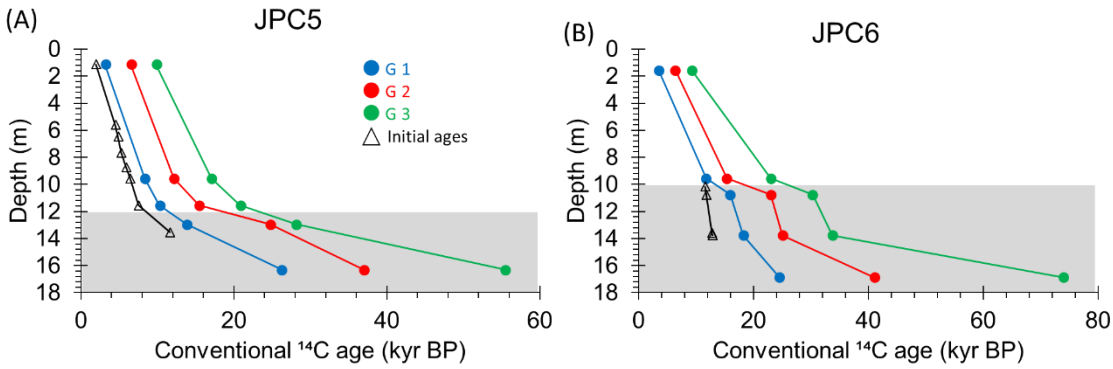

Fig. 2-7. Distribution of conventional ^{14}C ages of the G1-G3 peaks with core depth. Blue, red and green circles show ages of G1, G2, and G3, respectively. Black triangles show the initial ages (Suppl. Table 1). Deglacial sediments are shaded.

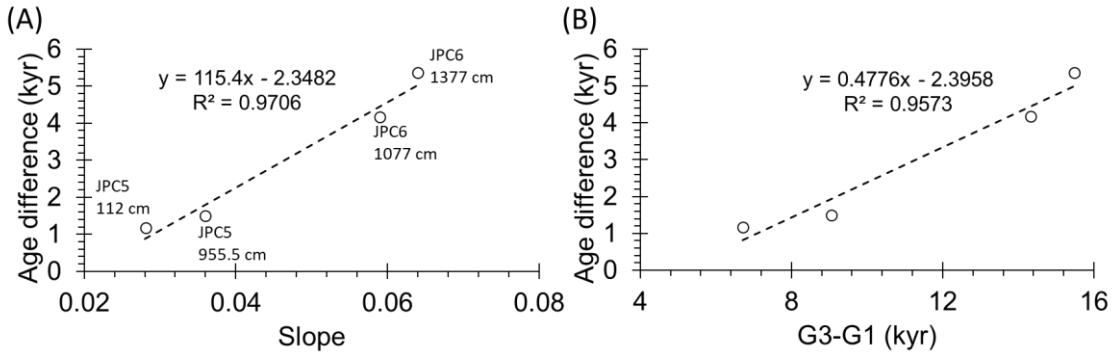

Fig. 2-8. Relationship between the slope of the conventional RP ^{14}C ages to pyrolysis temperature and the initial-G1 ^{14}C age difference (A) and between the G3-G1 components and the same age difference (B).

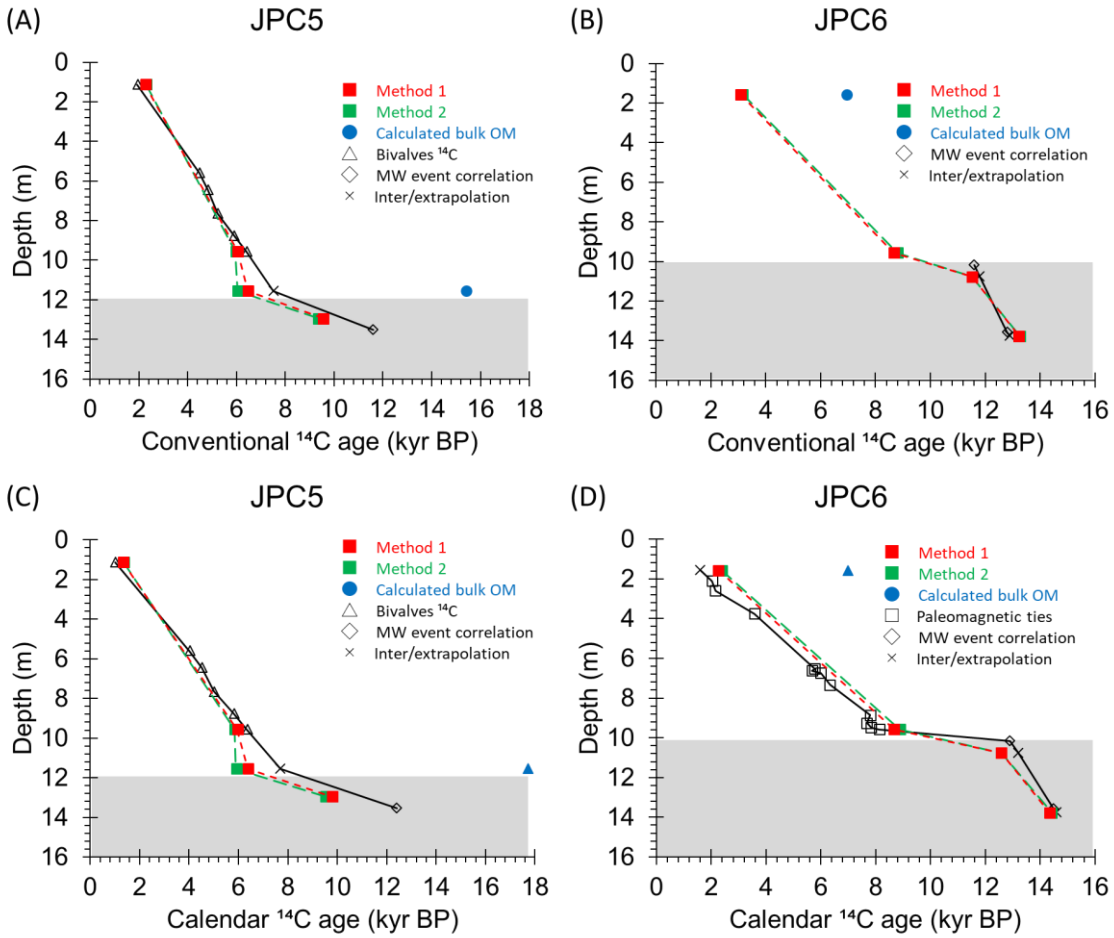

Fig. 2-9. Comparison of the initial ages (Suppl. Table 1) and the RP-based conventional and calendar ^{14}C ages obtained by the two estimation methods (red and green squares) for cores JPC5 (A, C) and JPC6 (B, D). Blue circles show calculated TOC ^{14}C ages. Deglacial sediments are shaded.

CHAPPTER III.
Event Stratigraphy of Deglacial Sediments in the Western Arctic

3.1. Introduction

Paleoceanographic research in the Arctic Ocean began by Russian scientists using ice island stations in the 1950s (Belov and Lapina, 1961). Subsequently, using the ice island station T-3, American scientists collected sediment cores from the Canadian Basin between 1952 and 1978. Based on the description of the cores, the initial stratigraphy of center Arctic sediment was established (Clark, 1970, Clark et al., 1980). A paleomagnetic reversal in the units J to M was correlated to the Brunhes–Matsuyama boundary (Fig. 3-1; Clark, 1970). However, this age model was inconsistent with the results of the subsequent ^{14}C dating studies (e.g. Darby et al., 1997; Poore et al., 1999). Later, changes in Mn content and sediment color were assumed to correspond to the oxygen isotope stages (Jakobsson et al., 2000). If this age model is correct, paleomagnetic change is correlated with geomagnetic excursions rather than geomagnetic reversals (Jakobsson et al., 2000). This assumption was proved by the Arctic Coring Expedition (ACEX) of the central Arctic Ocean (Backman et al., 2005).

The Mn-rich brown layer and the Mn-poor gray layer correspond to the warm interglacial/interstadial and cold glacial/stadial periods, respectively (Jakobsson et al., 2000; Backman et al., 2009; Polyak et al., 2004, 2007). However, in the wester Arctic Ocean, the bottom age of the Holocene brown layer tends to be older in offshore cores

(Jang et al., 2013), suggesting that this color stratigraphy has a limitation as a chronological method.

Detrital dolomite-rich layers exist in Arctic Ocean sediments and are useful for stratigraphic correlation (Darby et al., 1997; Bischof et al., 1996). The provenance of dolomite is limited in the Canadian Arctic Archipelago region, and detrital dolomite is indicative of transportation by iceberg discharges from the Canadian Arctic Archipelago (Stein et al., 2010a). Moreover, the provenance of the sediment in the Arctic Ocean was discussed based on terrestrial-origin OM composition (Yamamoto et al., 2008; Yamamoto and Polyak, 2009), the composition of oxide minerals (Darby et al., 2002) and mineral composition (e.g., Krylov et al., 2008; Kobayashi et al., 2016; Yamamoto et al., 2017). Application of mineral and OM analyses can provide more key beds for correlation and contribute to more precise stratigraphy.

In this study, we analyzed the ice rafted debris (IRD) abundance, grain size distribution, mineral composition, total organic carbon (TOC), total sulfur (TS), total nitrogen (TN) and glycerol dialkyl glycerol tetraethers (GDGTs) to establish the stratigraphy of western Arctic Ocean sediment.

3.2. Material and methods

3.2.1. The study area

In the western Arctic Ocean, the main ocean current systems consists of the Beaufort Gyre (BG) that flows clockwise along the Beaufort Sea, Chukchi Borderland to central Arctic, the Transpolar Drift (TPD) that flows from the eastern Siberian Sea to the Fram Strait, and the Bering Strait Inflow (BSI) that flows from the Bering Sea through Bering Strait into the Chukchi Sea (Fig. 3-2) (Coachman and Aagaard, 1988).

The seafloor topography of this area includes the Chukchi continental shelf and slope, the Northwind Ridge, the Chukchi Plateau, the Mendeleev Ridge, the Northwind Basin and the Chukchi Basin. The North Wind Ridge, the Chukchi Plateau, the North Wind Basin, and the vicinity of the Chukchi Basin are collectively called Chukchi Borderland (Fig. 3-2).

3.2.2. Samples

Core ARA02B 03A-GC (450 cm long) was retrieved during the RV "Araon" ARA02B expedition in 2011 from the Northwind Basin continental margin at a water depth of 455 m (Figs. 3-2, 3-3; Table 3-1). Cores ARA03B 02A-GC (495 cm long), 02B-GC (362 cm long), 08-GC (362 cm long) were retrieved from Northwind Basin at water

depth of 856, 375 and 2130 m, respectively (Figs. 3-2, 3-3; Table 3-1). Core 28A-GC (566 cm long) was retrieved during the ARA03B expedition in 2012 from the Mendeleev Ridge at a water depth of 1179 (Figs. 3-2, 3-3; Table 3-1). Cores HLY0501 05JPC (1600 cm long) and 06JPC (1800 cm long) were retrieved during the Healy-Oden Trans Arctic Expedition 2005 (HOTRAX'05) (Darby et al., 2005) from the Alaskan margin at water depth of 200 and 300 m, respectively (Figs. 3-2, 3-3; Table 3-1).

3.2.3. Methods

Approximately 1 g of sediment sample was soaked in the hot water in a beaker for 1 hour. The emulsion was screened by a 63 μm sieve. The fraction of >63 μm (sand) was transferred on the paper filter and dried in an oven at 60°C. After drying, the fraction was weighed. The fraction of <63 μm (clay and silt) stood overnight, and the supernatant was discarded by decantation. The residue was dried in an oven at 60°C.

About 0.03 g of the <63 μm fraction was soaked in the ion-exchanged water in a centrifuge tube for a couple of days. The grain size of the <63 μm fraction was analyzed using a HORIBA LA-920 laser scattering particle size distribution analyzer (0.02–2000 μm range; 2 repeat number; 0.2 % $Na_4P_2O_7 \cdot 10H_2O$ carrier fluid).

The <63 μm fraction was pulverized using an agate mortar and agate pestle. The

powdered sample was mounted on a glass plate. Semi-quantitative analysis of mineral composition was conducted using a MAC Science MX-Labo X-ray diffractometer equipped with a CuKα tube and monochromator. A tube voltage of 40 kV and current of 20 mA were used. Scanning speed was 4°2θ/min, data sampling step was 0.02°2θ and X-rayed from 2 to 40° 2θ in routine analysis and 0.4° 2θ/min, data sampling step was 0.01°2θ and X-rayed from 24 to 30° 2θ in the detailed analysis. The background-corrected diagnostic peak intensity was used for semi-quantitative evaluation of abundance for each mineral. Relative XRD intensities of quartz at 20.8°, kaolinite at 24.9°, chlorite at 25.2°, plagioclase at 27.9° and dolomite at 30.9° were determined for semi-quantification.

Mineral compositions of the >63 μm and <63 μm fractions were observed using a stereo microscope and a polarization microscope, respectively.

TOC, TN, TS and $\delta^{13}C$ of TOC were analyzed for the 02A, 02B and 28A cores. The <63 μm fraction was pulverized using an agate mortar and a pestle to make a fine powder. About 10 mg of sample was weighed in a tin cell for TOC, TN, and $\delta^{13}C$ analysis, and 1N hydrochloric acid was added to remove inorganic carbonate. After drying overnight, a tin cell was wrapped. Approximately 30 mg of sample was weighed into a silver cell for TS analysis, and about 1-2 g of vanadium oxide was added to wrap the silver cell, which was then wrapped in a tin cell. Analyzes were performed using an Euro Vector's elemental

analyzer EuroEA3000 and GV Instruments' stable isotope mass spectrometer Iso Prime EA. The $\delta^{13}C$ is expressed in parts per thousand compared to the isotope ratio of the reference material Vienna Pee Dee Belemnite (VPDB), and the accuracy of measurement is ± 0.1 ‰.

About 2 g of freeze-dried sediment was extracted three times with a DIONEX high-speed solvent extraction system ASE-200 (solvent: dichloromethane/methanol 3/2, carrier gas: nitrogen, temperature: 100 °C, pressure: 1000 psi, time: 10 minutes). The extracted lipids were concentrated, dried under nitrogen gas stream, and 0.25 ml of hexane was added. The extract was fractionated into four fractions (F1, F2, F3 and F4) by flowing four kinds of solvents with different polarities by silica gel (5 % H_2O) column chromatography. The hydrocarbon fraction F1 was eluted with 3 ml hexane, the polycyclic aromatic hydrocarbon fraction F2 was eluted with 3 ml hexane/toluene (3:1 v/v), the ketone fraction F3 was eluted with 4 toluene and the alcohol and fatty acid fraction F4 was eluted with 3 ml of toluene/methanol (3:1 v/v). The F4 fraction was analyzed with an Agilent liquid chromatograph 1260 Infinity 6130 quadrupole mass spectrometer (LC/MS). The LC column was a cyano column (length: 150 mm, diameter: 2.1 mm, particle diameter: 3.0 μm) manufactured by Alltech, and the column temperature was set to 30 °C. First, hexane /isopropanol (99:1 v/v) was flowed at 0.2 ml/min for 5

minutes, and the isopropanol ratio was increased to 1.8 % so that the flow was continued for 45 minutes. Then, hexane/isopropanol (90:10 v/v) was flowed in reverse direction at 0.2 ml/min for 10 minutes to wash. The sample that passed through the column was ionized by atmospheric ionization and introduced into MS. MS was set to the selected ion monitoring mode; *m/z* 743.7 for C_{46} GTGT internal standard, *m/z* 1292.3, 1296.3, 1298.3, 1300.3 and 1302.3 for isoprenoid GDGTs and *m/z* 1018, 1020, 1022, 1032, 1034, 1036 and 1050 for branched GDGTs. The concentration of each GDGT was determined as follows:

GDGT concentration (μg/g) = (amount of internal standard) × (compound peak area) × (response factor) / (peak area of internal standard) × (weight of sediment),

The Cyclisation of Branched Tetraethers (CBT) (Weijers et al., 2007), the Methylation of Branched Tetraethers (MBT') (Peterse et al., 2012) and Branched and Isoprenoid Tetraether (BIT) (Hopmans et al., 2004) were calculated by the following formulas:

CBT＝－log{([GDGT-Ib]＋[GDGT-IIb]) / ([GDGT-I]＋[GDGT-II])},

MBT’＝([GDGT-I]＋[GDGT-Ib]＋[GDGT-Ic]) / ([GDGT-I]＋[GDGT-Ib]＋[GDGT-Ic]＋[GDGT-II]＋[GDGT-IIb]＋[GDGT-IIc]＋[GDGT-III]),

BIT＝([GDGT-I]＋[GDGT-II]＋[GDGT-III]) / ([GDGT-I]＋[GDGT-II]＋[GDGT-III]＋[Crenarchaeol]).

3.3. Results

3.3.1. Lithology and color

The color of the sediment was mainly alternating between brown (B) layer and gray to olive gray (G) layer (Fig. 3-3) (Polyak et al., 2004). In cores 03A, 02B, JPC5 and JPC6, the B1 and G1 layers were recognized. In cores 28A and 02A, the B1 to the G2 layers were recognized. In core 08, the B1 to B5 layers were recognized. Distinct purplish (P) layer were recognized within the G1 layer of cores 02A, 03B and 08 (Fig 3-3). The B layers were sandy silt, the G layers were clayey silt, and P layers were silt containing sand (Fig. 3-3). The sediment of B and G layers showed higher L* than the sediment to the P layer (Fig. 3-4). The sediments of the B layer showed higher a * and b * than those of the G layer, and the sediments of the P layer showed intermediate values between those of the B and G layers (Fig. 3-4).

3.3.2. The abundance of >63 μm fraction (IRD abundance) and the grain size distribution of the <63 μm fraction

The IRD content was remarkably high in the B layer during the last glacial period (Figs. 3-5; 3-6). The Holocene section did not contain much IRD (Fig.3-5). On the other hand, in G layers, the IRD content was high (Figs. 3-5; 3-6). In the layer with abundant IRD (>63 μm fraction), the mean grain size the <63 μm fraction was generally coarse, but exceptionally in the P layer, the mean grain size of the <63 μm fraction was high despite of low IRD content (Fig. 3-5).

3.3.3. Mineral composition

The dolomite/quartz ratio showed high values in the B layer except for the lower part of 28A and 08A cores (Figs. 3-7; 3-8A). The B layer has a high content of IRD (>63 μm fraction) and shows the high dolomite/quartz, while the G and P layers have low contents of IRD and shows the low dolomite/quartz ratio (Fig. 3-8A). The kaolinite/illite ratio is high in the B layer sediments with high IRD content and the high dolomite/quartz ratio (Fig. 3-9; 3-8B). The kaolinite/illite ratio is highest in the P layer sediments in the 02A, 02B, 03B and 08 cores (Fig. 3-8B). The G and P layers can be distinguished by the kaolinite/illite ratio of 0.24 (Fig. 3-8B).

3.3.4. Organic matter

TOC, TS, and TN showed high values in the B1 and P layers in the 02A, 02B and 08 cores (Figs. 3-10, 3-11). TOC, TS, and TN tended to show higher values in the same layers in different cores (Figs. 3-10, 3-11, 3-12). TOC and TS are remarkably higher in the P layer sediments than the B and G layer sediments (Figs. 3-10, 3-11, 3-12). The $\delta^{13}C$ value shows maxima in the B1 in all study cores (Figs. 3-10, 3-11).

3.3.5. GDGTs

Isoprenoid and branched GDGTs showed synchronous variation between the 02A core (Fig. 3-10). The P layer in the 02A core showed high branched GDGT concentration (Fig. 3-10). A CBT and MBT' plot indicates that most samples are distributed in the region of soil OM (Fig. 3-13A; Park et al., 2014), suggesting that the abundant branched GDGTs in P layer sediments are soil bacteria origin (Fig 3-13B).

3.4. Discussion

3.4.1. Stratigraphic correlation based on grain size and mineral composition

The sediments of cores were correlated based on lithological parameters, i.e., IRD (>63 μm fraction) and the mean grain size of the <63 μm fraction. The sediments of IRD layers

in the B1 layer contain about 1 % of IRD, their mean grain size was small and sorting was worse (Fig. 3-5, 3-9, 3-14). On the other hand, the sediments containing 5─60 % of IRD were deposited mostly in the B layers (Fig. 3-5, 3-9). Darby et al. (2009b) reported that distal sediments had smaller mean grain sizes with worse sorting (Fig. 3-14). In distal offshore areas, sorting is poor due to the increased contribution of sediment carried by nepheloid flow (Darby et al., 2009b). The mean grain size and sorting of B and G layers in the 02A core are distributed in a range similar to the sediments on the Alaska margin in the Darby et al. (2009b) plot, suggesting that nepheloid flow contribute to sediment transport (Fig. 3-14). On the other hand, the P layer sediments were plotted in a different area from the modern sediments investigated by Darby et al. (2009b) because the mean grain size was larger and sorting was worse (Fig. 3-14). It may have been transported by a different mechanism than common transport processes, such as suspended matters by nepheloid flow or ice (sea ices and icebergs). Sediments transported by icebergs are coarser than those transported by sea ice, because sea ices trap grains floating in the water, while icebergs grab rock fragments from glacial basements (Mullen et al., 1972; Darby et al., 2011). Thus, lower IRD content in the B1 layer indicates sediment transportation by sea ice and higher IRD content in the G layers indicates sediment transportation by icebergs (Mullen et al., 1972; Darby et al., 2011).

The kaolinite/illite ratio showed a high value in the layers with the dolomite/quartz ratio in most cases in the G layers (Figs. 3-9, 3-10). Such layers with the dolomite/quartz ratio over 0.07 and the kaolinite/illite ratio over 0.1 are defined as dolomite and kaolinite-rich (DK) layers in this study (Fig. 3-7; DK1-K10). However, the P layer had a high kaolinite/illite ratio with no dolomite. This layer was defined as the kaolinite-rich (K) layer (Fig3-9). RF ^{14}C dating indicated that the ages of bottom and top of this layer are 14,500 and 13,200 years ago, respectively, corresponding the onset and end of the BA period (Chapter 2).

3.4.2. Provenance of the DK layers

Early Paleogene dolomite bed rocks are distributed in the inland Canadian Arctic Archipelago, the lower Makenzie river basin, the southern margin of the Hudson Bay, the Wrangel island, the Kotelny island, the Severnaya Zemlya and the Olenek river basin (Fig.3-15; Dalrymple and Maass, 1987; Darby et al., 1989; Trettin, 1991; Gordeev and Sidorov, 1993; Petrov et al., 1995; The Atlas of Canada, 2009). The dolomite IRD was thought to be derived from the Canadian Arctic Archipelago (Bischof et al., 1996; Bischof and Darby, 1997; Philips and Grantz, 2001). Kaolinite is abundantly born in the Mesozoic sedimentary rock (Biscaye, 1964; Naidu and Mowatt, 1984), which is distributed in the

western margin of the Canadian Arctic Archipelago, the Makenzie river basin, the northern and western Alaska and the western Canada (Fig.3-15; Naidu and Mowatt, 1984; The Atlas of Canada, 2009). During the LGM, the ice sheet covered both the inland of the Canadian Arctic Archipelago and the Makenzie River basin (Ruddiman, 2001). The co-occurrence of kaolinite and dolomite in the DK layer, thus, suggests that the sediments of the DK layer was delivered from the inland of the Canadian Arctic Archipelago of the Laurentide ice sheet, further supporting the hypothesis that dolomite IRD originated from the Canadian Archipelago (Bischof et al., 1996; Bischof and Darby, 1997; Philips and Grantz, 2001) from a new aspect of mineralogy.

3.4.3. The characteristics and provenance of the K layer (=P layer)

The sediments of the K layer (P layer) is massive has sharp contacts at the bottom and top of the layer (Fig. 3-10). The <63 μm fraction are coarser and the sorting is worse than those of the B and G layers with no dolomite (Fig. 3-8, 3-10). The grains are angular. This lithological characteristics are unique in western Arctic sediments and not seen in modern sediments in the study area, which are mostly transported by sea ice (Fig. 3-14; Darby et al., 2009b, 2011). No IRD (>63 μm fraction) and the presence of coarse and unsorted silt in the K layer suggests that the sediments were transported by the strong stream of turbid

water, like flooding deposits (Darby et al., 2009b, 2011). Angular grains in the K layer also suggests the origin of river discharge with high energy (Krumbein, 1940; Darby et al., 2009b, 2011).

The TOC and TS were higher values than those of the other layers (Fig. 3-12A). In addition, the scatter plots of TOC and TN show that the K layer has a low nitrogen content relative to carbon (Fig. 3-12B). A high TS indicates that OM was decomposed in marine sediments and sulfidation by the sulfate-reducing bacteria occurred in an anoxic condition (Berner, 1982). When organic matter is decomposed, nitrogen compounds are denitrified and discharged from sediments as nitrogen gas (Kester et al., 1996). As a result, OM rich in carbon and sulfur and low in nitrogen is preserved in sediments.

Zhang et al. (2019) recently reported abundant coal fragments layers in the K layer in cores JPC5 and JPC6. The presence of coal fragments agrees well with the high TOC in the layer (Figs. 3-10, 3-11, 3-12). The coal fragments are fresh, indicating that coal seams were eroded rapidly and immediately delivered without chemical weathering nor oxidation to western Arctic. On the other hands, the abundant branched GDGTs in the K layer indicates the contribution of soil to the sediments. These lithological and geochemical characteristics of the K layer sediments suggests that they were transported by the strong stream of turbid water, and in the sediment source area coal and kaolinite-

bearing rocks are eroded and immediately delivered to ocean, and at the same time, surface soil was also widely eroded and delivered to ocean.

Both kaolinite and coal are abundantly born in Mesozoic sedimentary rocks in the northern and western Alaska and the western Canada (Fig. 3-15; Biscaye, 1964; Naidu and Mowatt, 1984; Flores et al., 2003; The Atlas of Canada, 2009). The Cretaceous Scholard Formation in Western Canada bears both kaolinite and coal, which is the most likely source of the K layer. This formation is distributed within the drainage basin of the Mackenzie River and outcrop area was located at the western margin of the Laurentide ice sheet during the BA period (Ruddiman, 2001). I suppose that the rapid melting of the western margin of the Laurentide ice sheet continued to produce the meltwater which eroded the outcrops of the Mesozoic sedimentary rocks by strong stream flow during the BA period. The data of Keigwin et al. (2018) indicated that freshwater discharge continued during the BA period (14.5-12.9 ka) (Fig. 3-16). Sedimentation rate at the Mackenzie Delta between 12.9 and 14.5 ka was extremely high (>1000 cm/kyr) in the Mackenzie delta (Fig. 1-4; Keigwin et al., 2018). These findings are consistent with our finding that Mackenzie-derived sediments delivered during the BA period are widely distributed in the western Arctic Ocean.

3.5. Conclusions

The stratigraphy of western Arctic Ocean sediments was established based on lithological and geochemical properties. Dolomite-rich layers are useful for high resolution correlation of western Arctic Ocean sediments. A unique kaolinite-rich layer (K layer) was recognized from the 13.2-14.5 ka intervals (BA period) in the western Arctic Ocean sediment sequence. The sediments of the K layer most likely originated from inland Canada through the proto-Mackenzie River. The sediment property suggests that the sediments were transported by strong water stream rather than sea ice/iceberg drifting.

Table 3-1 Core locations

Leg	Site	Cores	Latitude	Longitude	Water depth	Core length
ARA02B	03B	GC-01	75°07'02 N	166°20'33 W	455 m	450 cm
ARA03B	02A	GC-02	74°13'79 N	162°51'15 W	856 m	495 cm
ARA03B	02B	GC-02	74°08'73 N	163°16'29 W	375 m	362 cm
ARA03B	08	GC-03	76°36'55 N	161°12'74 W	2130 m	362 cm
ARA03B	28A	GC-03	76°13'11 N	179°50'15 E	856 m	450 cm
HLY0501	5	JPC	72°41’7 N	157°31’2 W	415 m	1628 cm
HLY0501	6	JPC	72°30’7 N	157°02’1 W	673 m	1554 cm

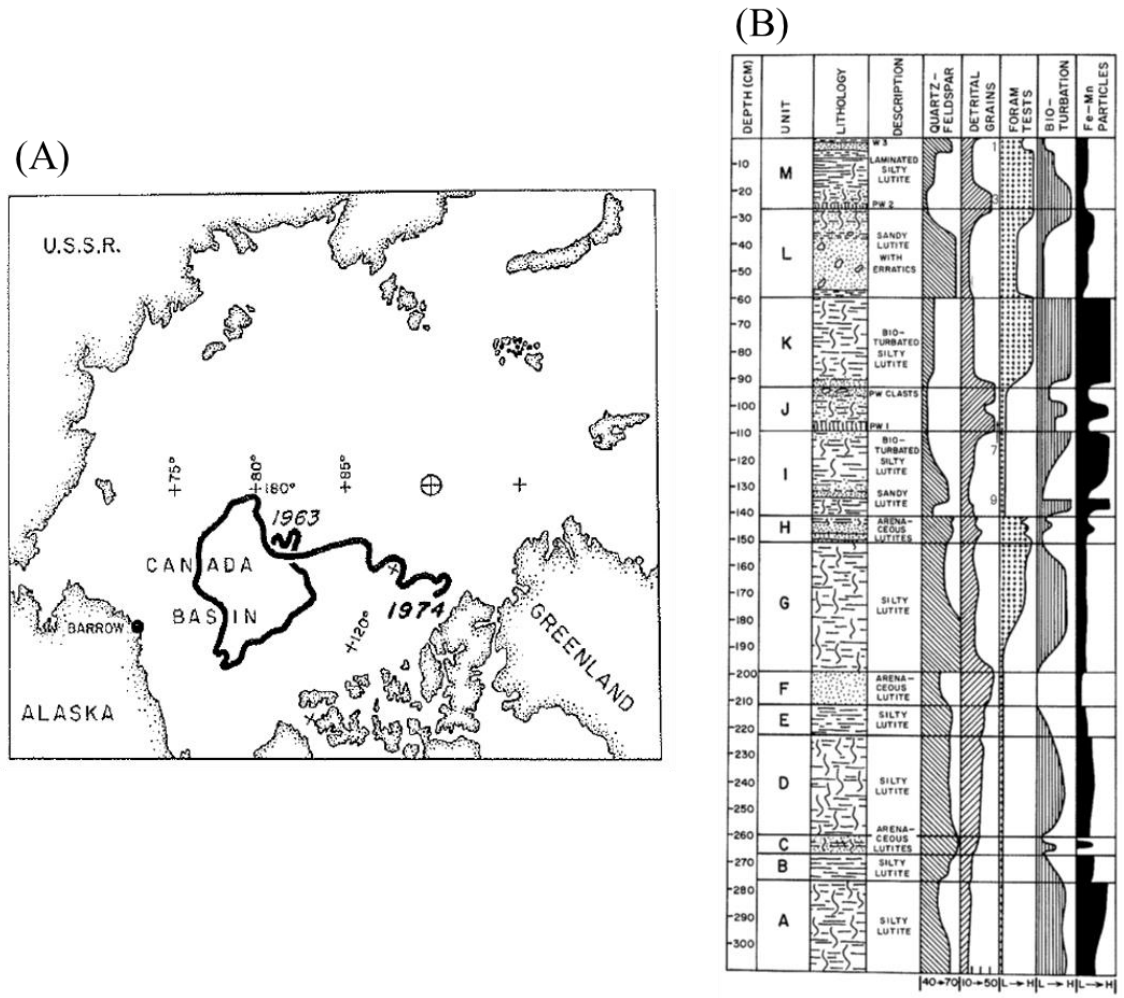

Fig. 3-1. The path of iceberg T-3 drift (A) and Canadian Basin sedimentary stratigraphy established from the lithology of recovered sediment cores (B) (Clark et al., 1980).

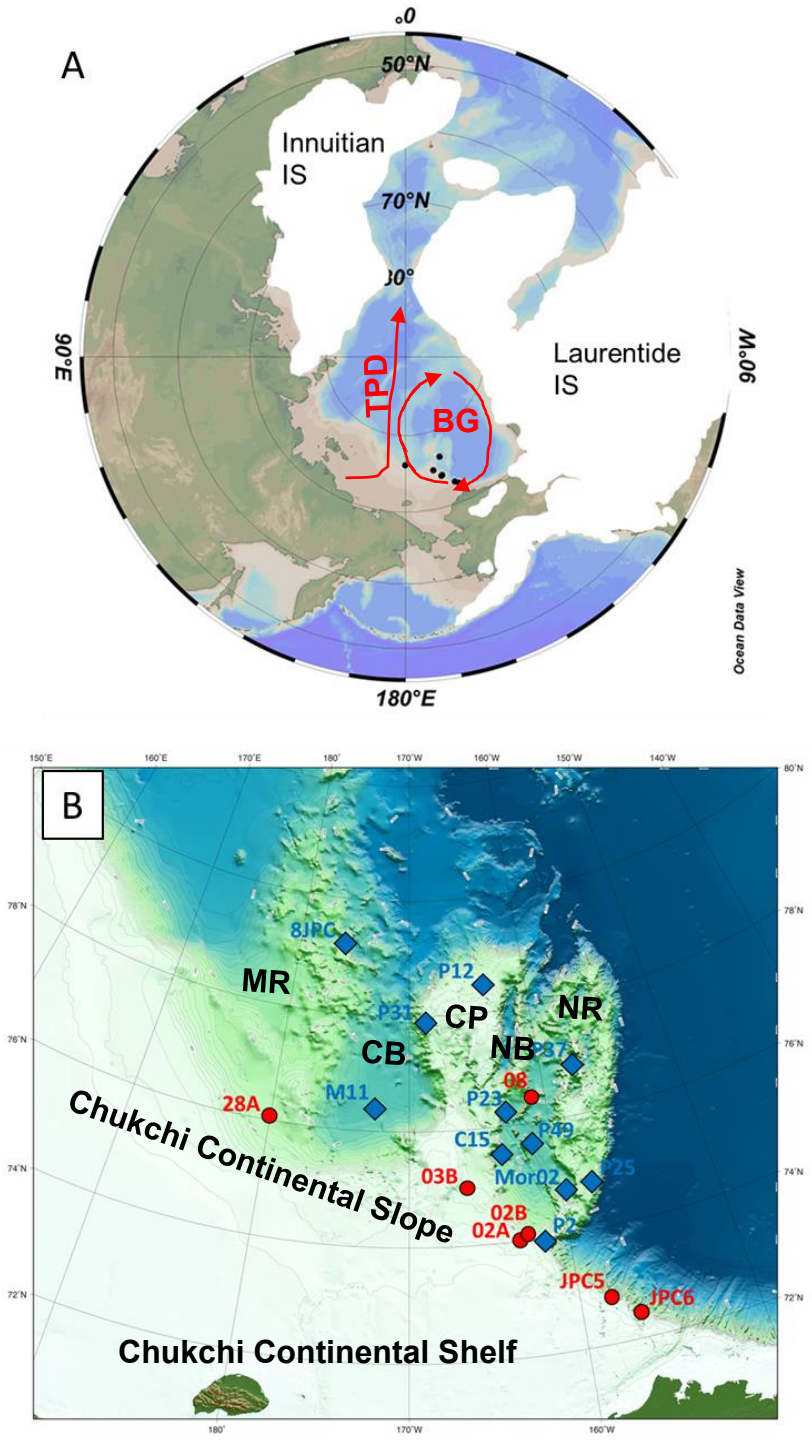

Fig. 3-2. Study area (A) and the locations of cores (B). The area covered with white in panel A indicates the extents of the LGM ice sheet (data from Ruddiman, 2001). Red circles in panel B indicate the study cores and blue diamond indicate the core of Zhang et al. (2019). TPD: Transpolar Drift, BG: Beaufort Gyre, MR: Mendeleev Ridge, CB: Chukchi Basin, CP: Chukchi Plateau, NB: Northwind Basin, NR: Northwind Ridge.

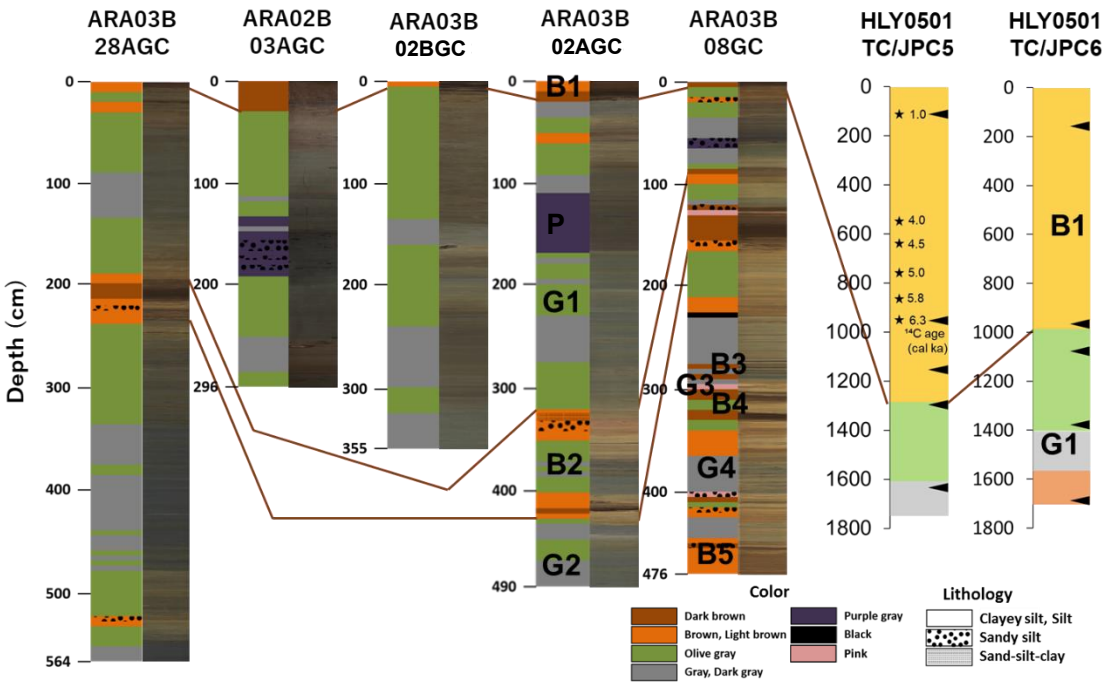

Fig. 3-3. The stratigraphy and photos of sediments for cores 28A, 03A, 02A, 02B, 08, JPC5 and JPC6 (ARA02B cruise report; ARA03B cruise report; MacKay et al., 2008; Darby et al., 2009b; Polyak et al., 2009). Classification of sediments based on color property was conducted in this study. Black triangles show the samples dated by RP ^{14}C method in Chapter 2. B: Brown layer, G: Gray layer, P: Purple layer.

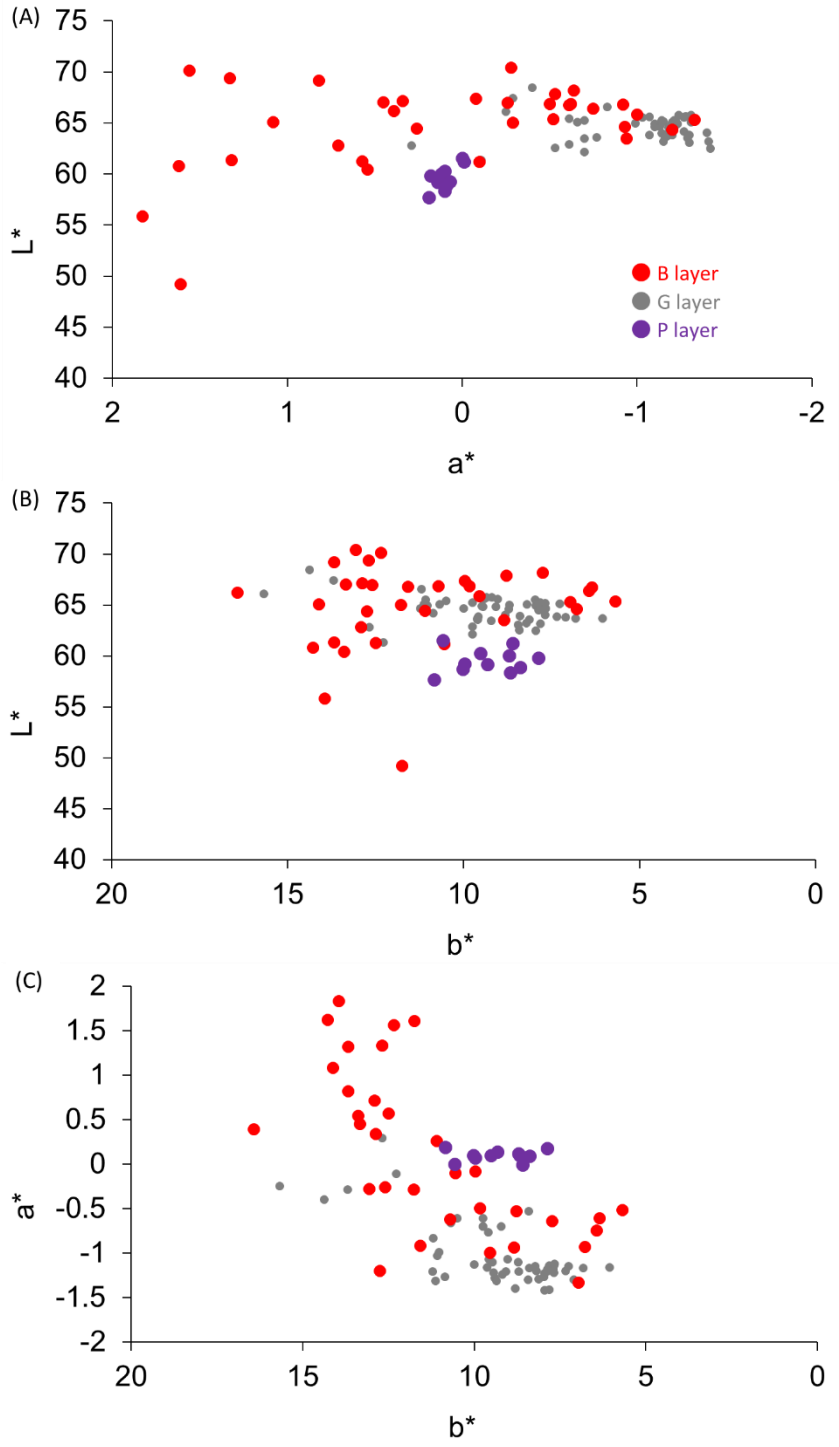

Fig. 3-4. Scatter plot of IRD (>63μm fraction) content and the mean grain size of the <63μm fraction for 02A core.

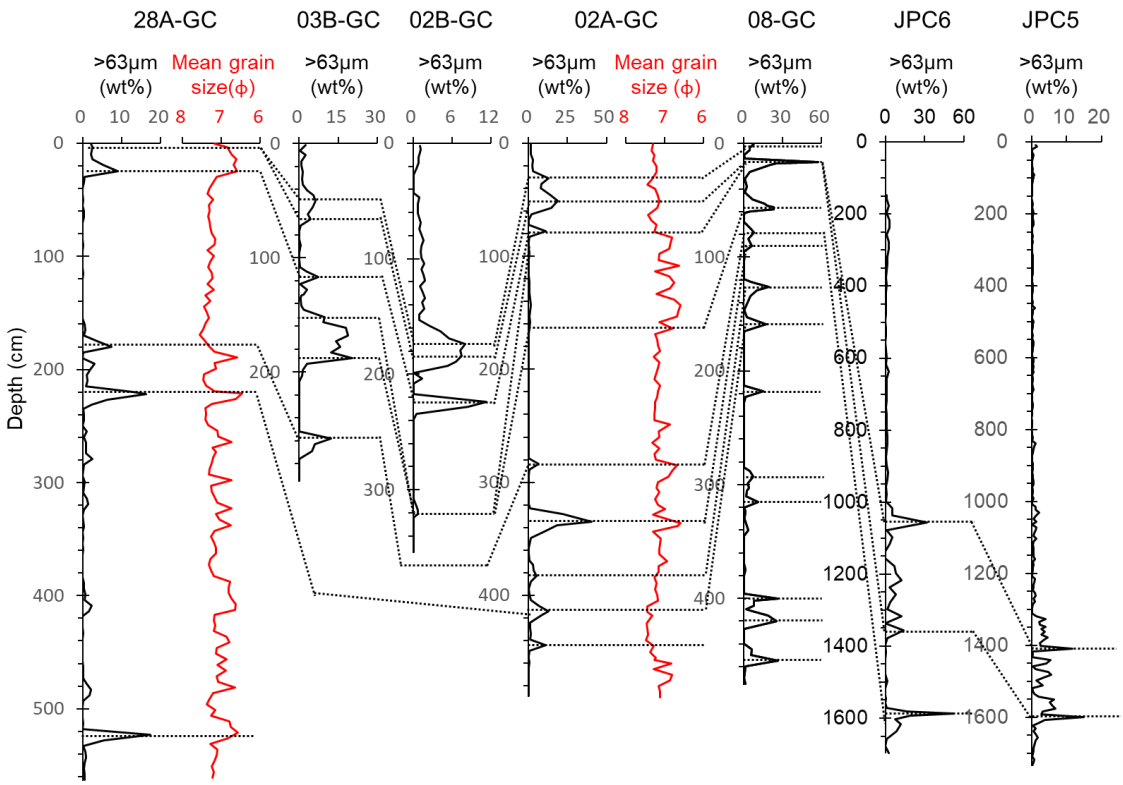

Fig. 3-5. IRD content (>63 μm fraction) and the mean grain size of the <63 μm fraction in cores 28A, 03A, 02A, 02B, 08, JPC5 and JPC6.

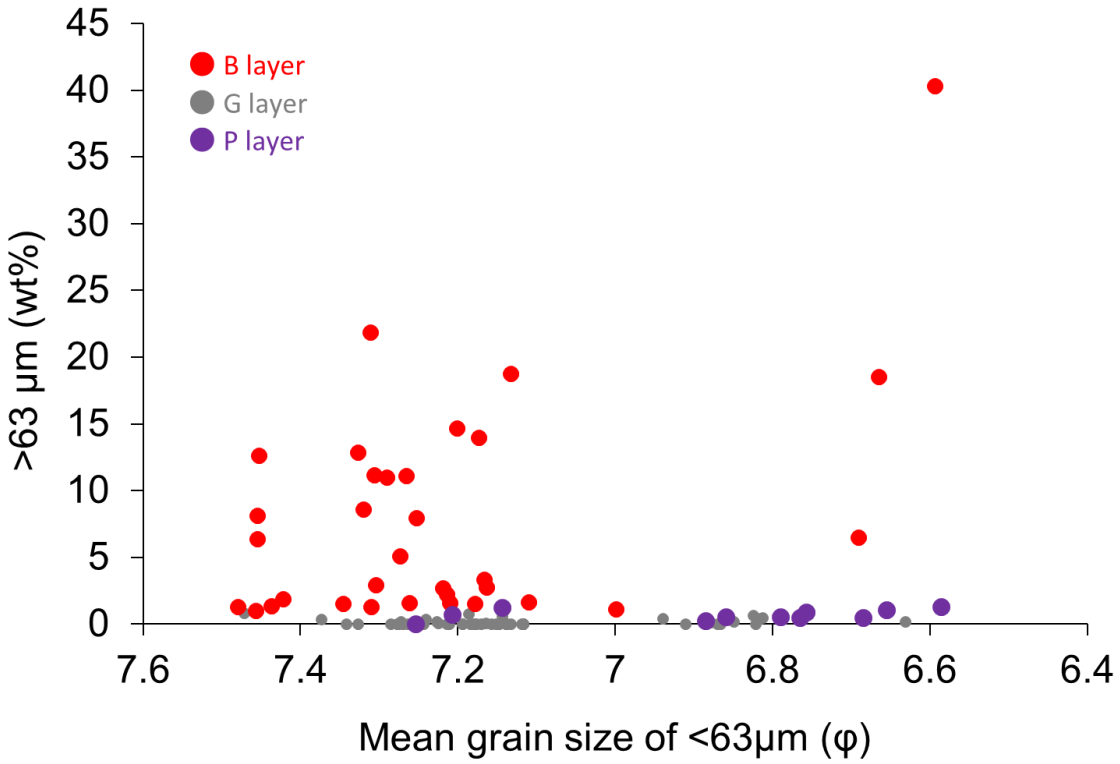

Fig. 3-6. Scatter plot of >63μm grain concentration and mean grain size of <63μm fraction of 02A core.

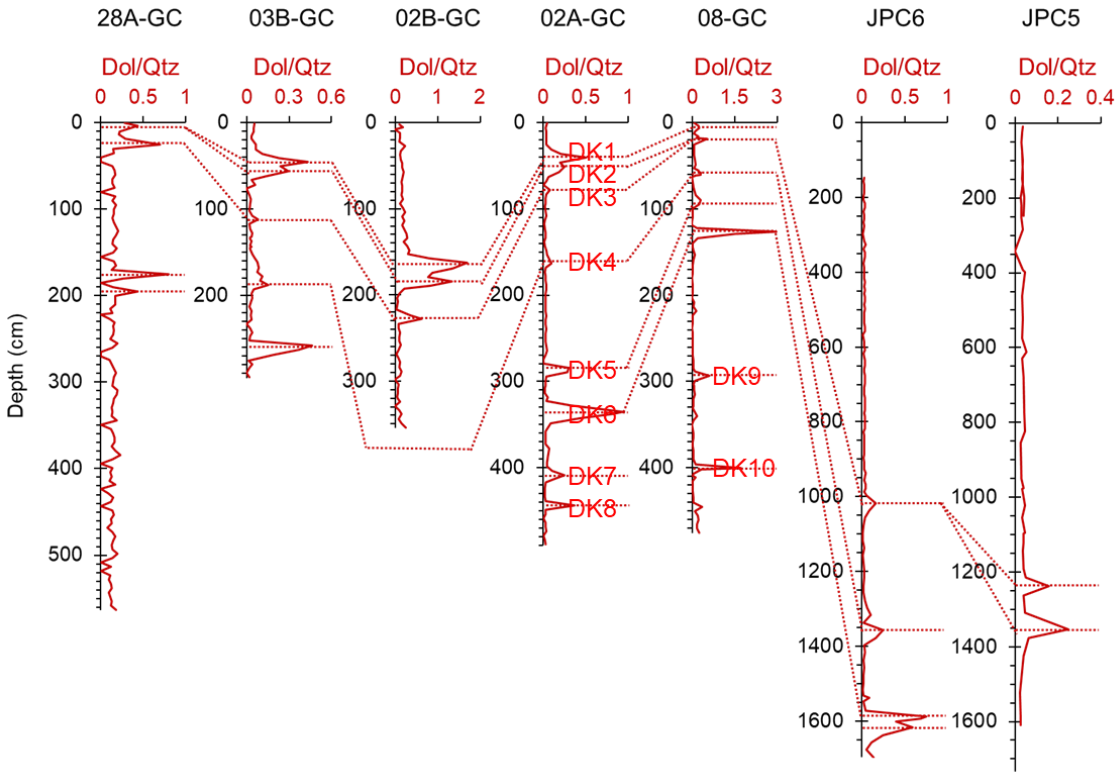

Fig. 3-7. The dolomite/quartz ratio in cores 28A, 03A, 02A, 02B, 08, JPC5 and JPC6. Red dot lines indicate the correlations between dolomite-rich layers.

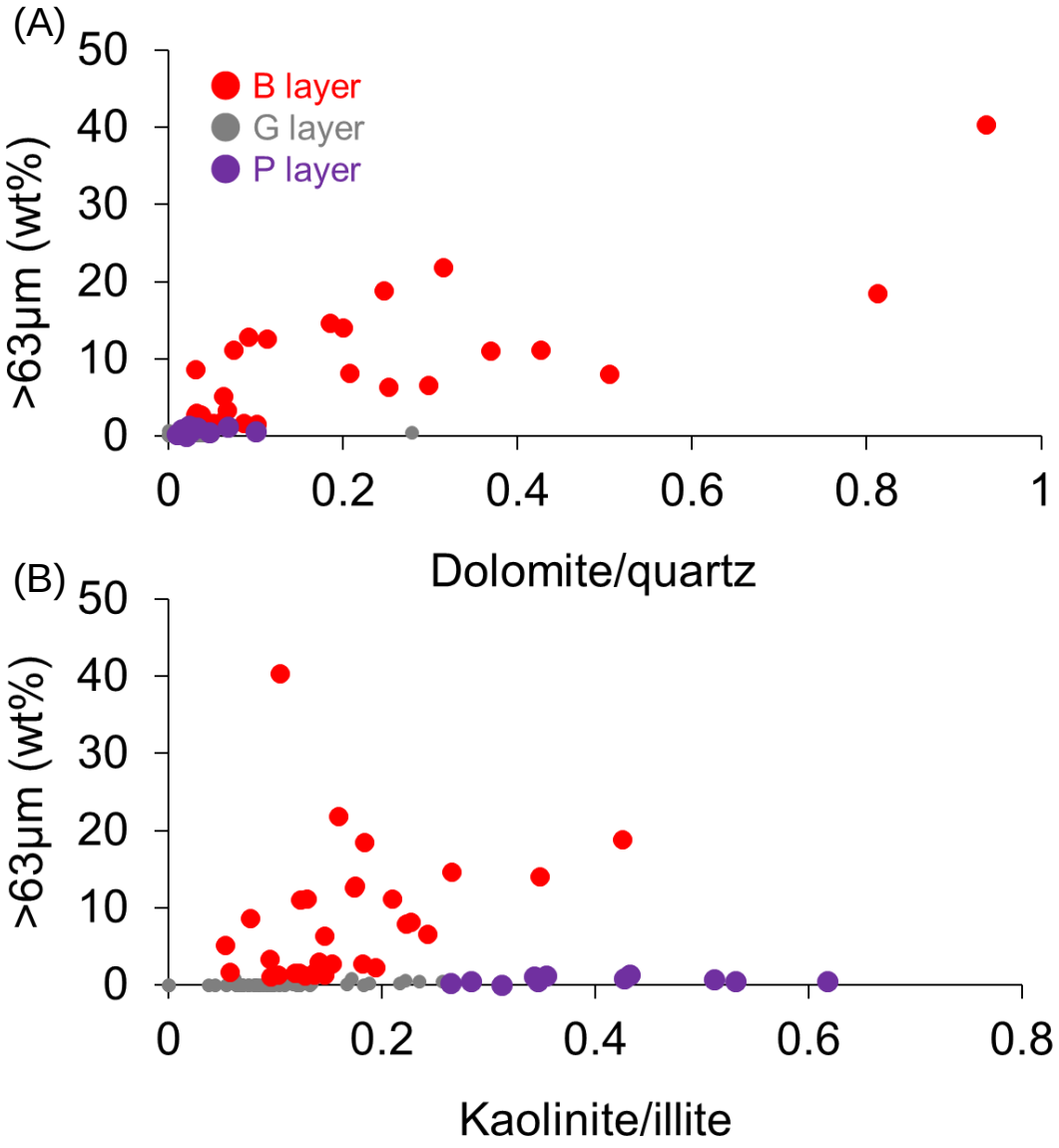

Fig. 3-8. Scatter plots of the IRD (>63μm fraction) content and the dolomite/quartz ratio (A) and the kaolinite/illite ratio (B) for 02A core.

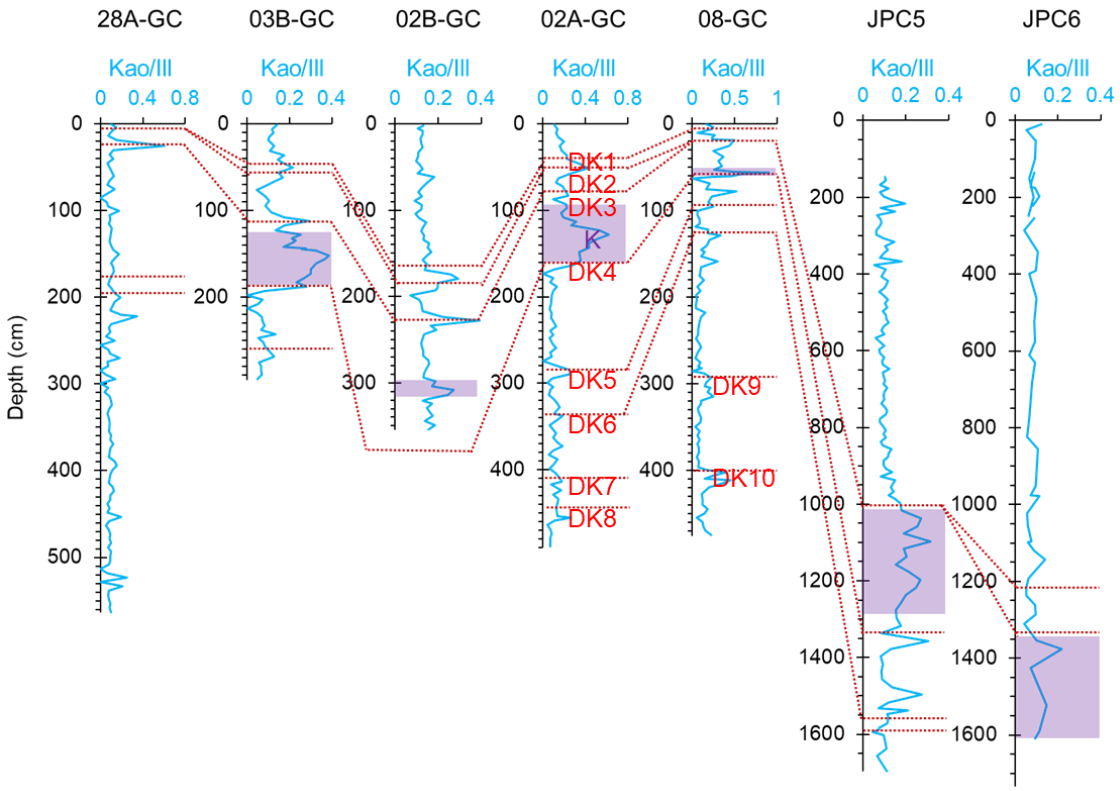

Fig. 3-9. The kaolinite/illite ratio in cores 28A, 03A, 02A, 02B, 08, JPC5 and JPC6. Red dot lines indicate correlations between dolomite-rich layers. Purple shade indicates the P layer (=K layer).

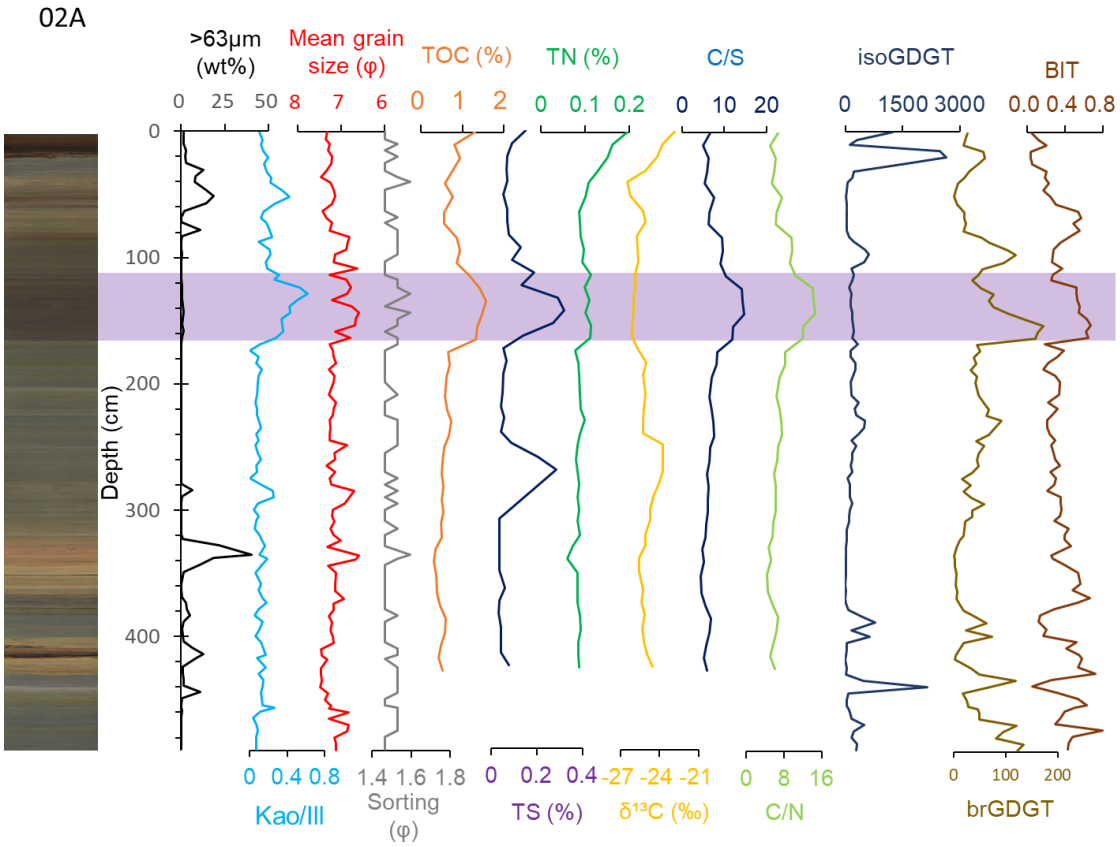

Fig. 3-10. Photo, IRD (>63 μm fraction) content, the mean grain size and sorting of the <63 μm fraction,, the kaolinite/illite ratio, TOC, $\delta^{13}C$, TS, TN, C/S, C/N, isoprenoid and branched GDGT concentration and the BIT in core 02A. Purple shade indicates the P layer (=K layer).

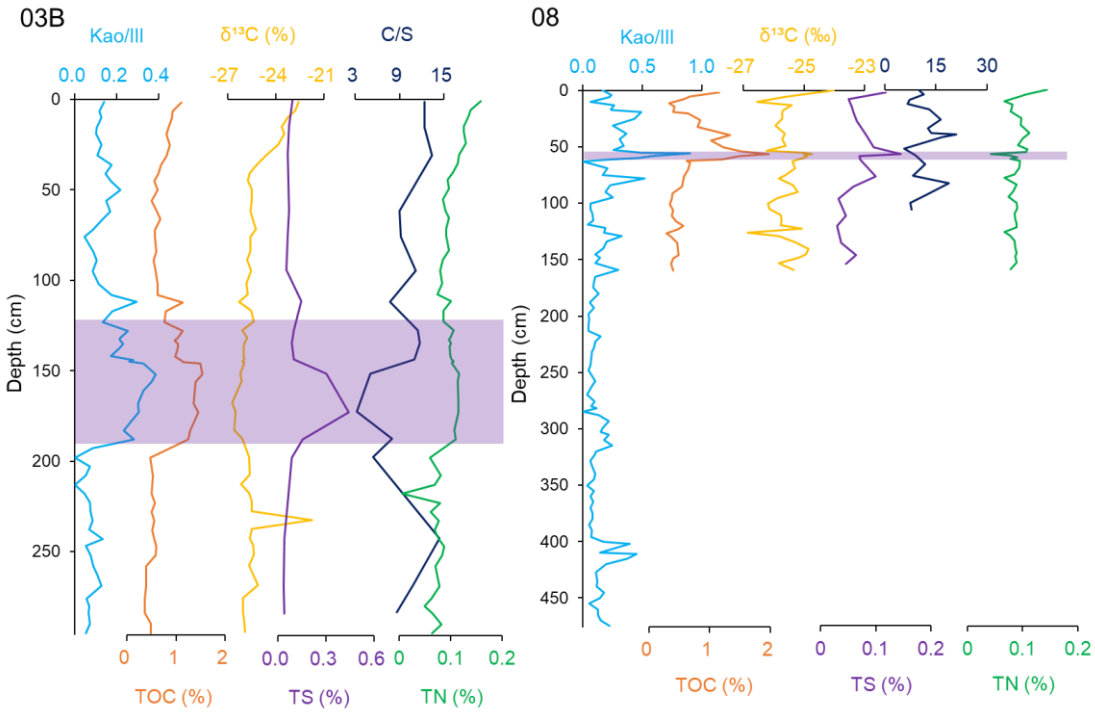

Fig.3-11. the kaolinite/illite ratio, TOC, $\delta^{13}C$, TS, C/S and TN in 03B and 08 cores. Purple shade indicates the P layer (=K layer).

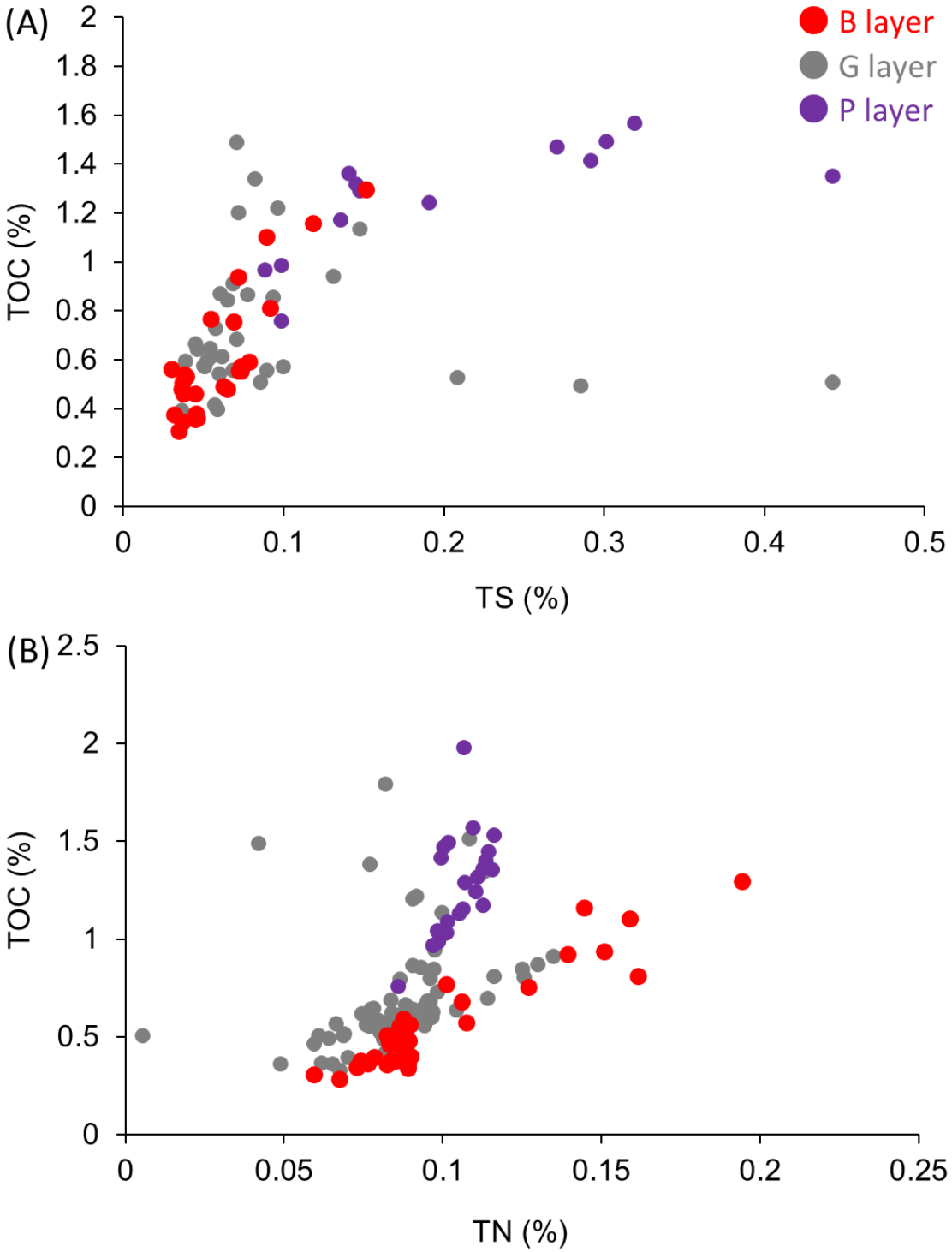

Fig. 3-12. Scatter plots of TOC and the TS (A) and the TN (B) of 02A, 03B and 08 cores.

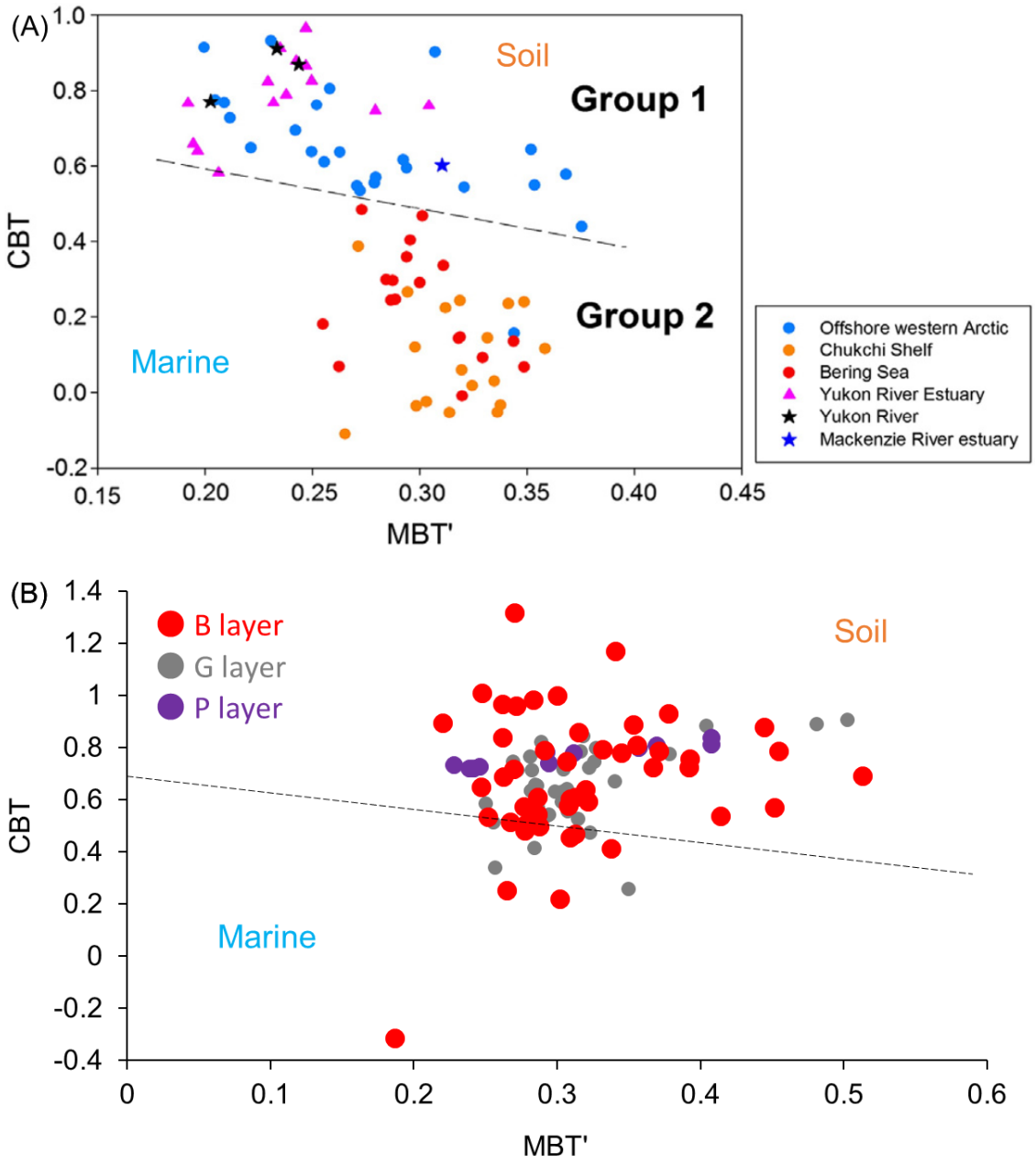

Fig. 3-13. Scatter plots of CBT and MBT' of Park et al. (2010) (A) and 02A core (B).

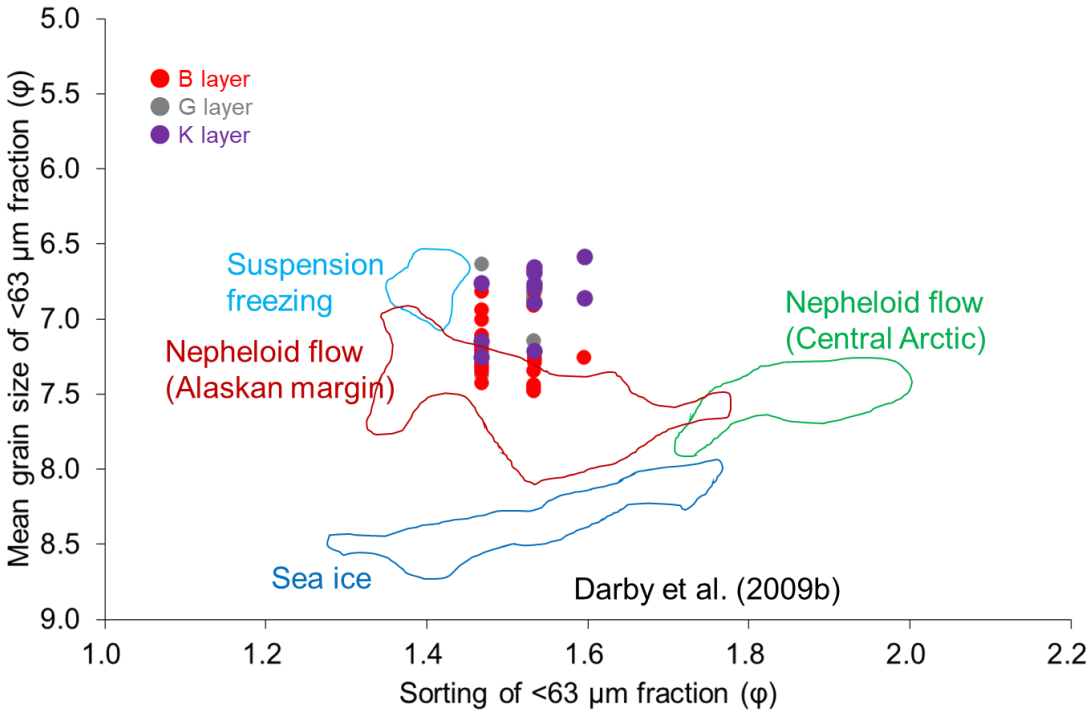

Fig.3-14. Scatter plot of mean grain size and sorting of data from 02A (this study) and Darby et al. (2009b).

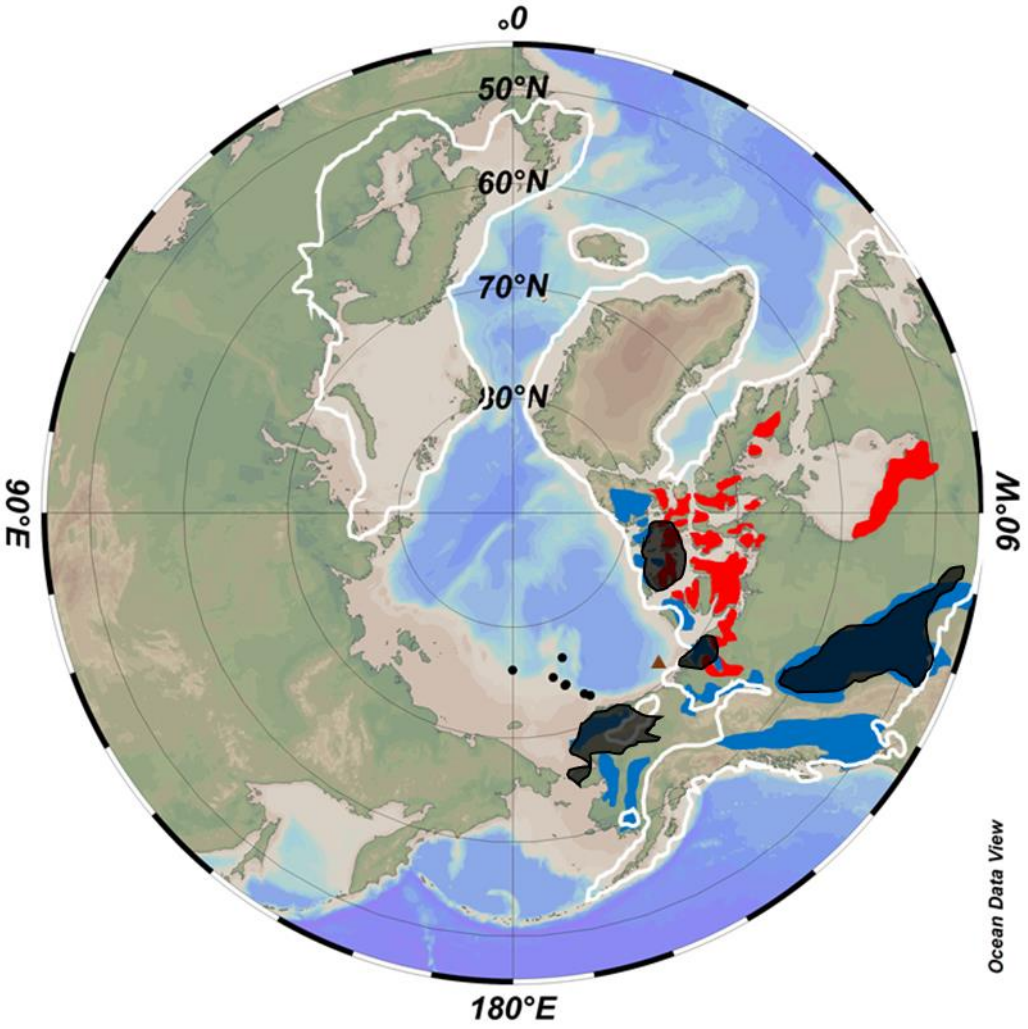

Fig. 3-15. Distribution area of dolomite (red), kaolinite (blue) and coal (black) bed rocks. White line indicate the extents of the LGM ice sheet (data from Ruddiman 2001).

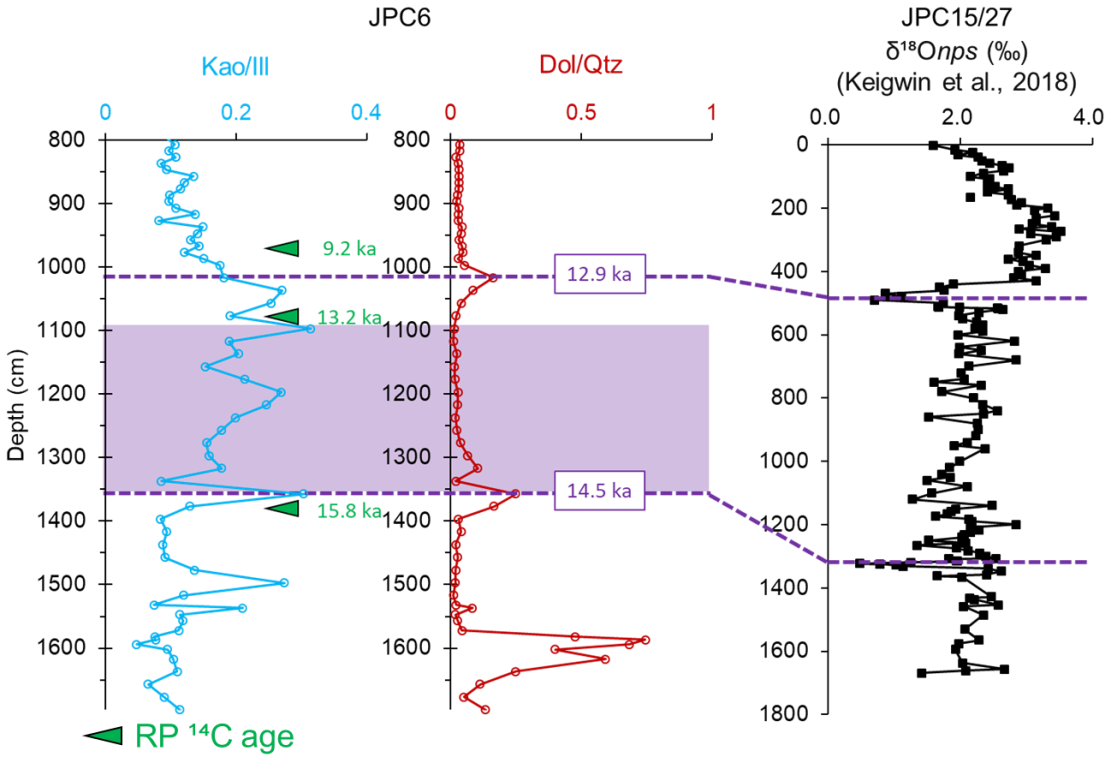

Fig. 3-16. Stratigraphic correlation based on dolomite/illite ratio and changes in $\delta^{18}O$ of planktonic foraminifera (Keigwin et al., 2018). Purple shade indicates the P layer (=K layer). Green triangles indicates the estimate ages by RP ^{14}C dating (See Chapter 2).

Chapter IV.
General Discussion

4.1. Introduction

Global sea level rose by 25m during the BA period (Fig. 4-1; Yokoyama et al., 2018). The freshwater inflow into the ocean during this period, however, did not affect the AMOC (Fig. 1-5; Ritz et al., 2013). An ocean model shows that the response of the AMOC to freshwater input is different depending on the route of freshwater from the Laurentide ice sheet (Condron and Winsor, 2012). In order to test this model, we need to know how much amount of freshwater flowed from the Laurentide ice sheet through different routes. A model study indicated that, at the onset of the Younger Dryas period, 50 % of freshwater from the Laurentide ice sheet discharged to the Gulf of Mexico via the Mississippi River, 30% to the western North Atlantic via St. Lawrence River, and 20% to the Arctic Ocean via the Mackenzie River (Tarasov and Peltier, 2005).

In this study, we estimated the amount of meltwater which flowed from the Laurentide ice sheet to the Arctic Ocean during the BA period. The minimum deposition area and thickness of the K layer deposited on the BA period, which was clarified in this study (Chapter 2 and 3), enables us to estimate the amount of freshwater required to transport this sediment.

4.2. Methods

From the deposition area and thickness of the K layer found in this study, the volume of sediment transported by meltwater during the BA period was estimated. Assuming the density of turbid water which carried the sediments, I obtained the amount of freshwater.

4.3. Results and discussion

The observed area of the K1 layer is 4.3×10^5 km^2 (Fig. 4-2). In order to calculate the area of the K layer, the map was divided into cells for each degree in longitude and latitude, and the number of cells of each latitude in the K layer deposition area was counted. The area of each area was calculated by multiplying the counted cell by the area of the cell at each latitude (Fig. 4-2). The thickness of the K1 layer was assumed to be 700, 300, 100 and 50 cm in Mackenzie River Delta, Alaskan margin, Chukchi continental margin and Chukchi borderland areas, respectively (Fig. 4-2). Total volume of K1 sediments is calculated by the following formula:

5×10^4 (km^2) $\times$ 7 (m) + 1.4×10^5 (km^2) $\times$ 3 (m) + 5.5×10^4 (km^2) $\times$ 1 (m) + 1.9×10^5 (km^2) $\times$ 0.5 (m) = 9.2×10^2 (km^3),

which is a minimum estimate, because it excludes the Canada Basin area which we suppose the deposition of the thin K layer. The calculated volume of the K layer is 9.2×10^2 km^3. Assuming the density of the K layer sediment is 1.6 t/m^3 (the value of central Arctic sediments from O'Regan [2007]), the total weight is 14.7×10^{11} t. This calculated volume corresponds to the 51 cm thick sediments covering the entire drainage area of Mackenzie River (1.8×10^6 km^2).

Since the K layer continued to deposit during the 1300 years of the BA period, the annual sediment discharge from the proto-Mackenzie River was calculated by the following formula:

$$1.47 \times 10^{12} \text{ (t)}/1300 \text{ (years)} = 11.3\times 10^8 \text{ (t/year)},$$

which is 9.4 times higher than the present average sediment discharge of Mackenzie River (1.2×10^8 t/year; Rachold et al., 2004). Sediment concentrations in the modern Mackenzie River increase with increasing river discharge (Carson et al., 1998). The amount of freshwater when the sediment is transported about 9 times the average is about 2 to 4 times the average (Cason et al., 1998). The freshwater runoff in the BA period can be calculated from the runoff from modern Mackenzie River (3.3×10^2 km^3/year; Rachold

et al., 2004) as follows:

3.3×10^2 (km^3/year) × 2 = 6.6×10^2 (km^3/year) (minimum),

3.3×10^2 (km^3/year) × 4 = 1.3×10^3 (km^3/year) (maximum)

Thus, the total amount of freshwater which inflowed through the proto-Mackenzie River to the western Arctic Ocean during the 1300 years of BA period is calculated to be $8.6 \times 10^5 \sim 1.7 \times 10^6$ km^3. This estimate includes the contributions of both meltwater and precipitation in the Mackenzie River basin. If the precipitation during the BA period was the same as that at the present (3.3×10^2 km^3/year), the volume of meltwater during the BA is estimated to be $8.6 \times 10^5 \sim 1.7 \times 10^6 - 4.3 \times 10^5 = 4.3 \times 10^5 \sim 1.3 \times 10^6$ km^3. Because the total area of the modern oceans is 3.6×10^8 km^2, the freshwater discharge through the proto-Mackenzie River to the western Arctic Ocean corresponded to sea level rise by 1.2 ~ 3.6 m. Since the sea level rise in the BA period was 25m (Yokoyama et al., 2018), the freshwater runoff from the Laurentide ice sheet to the Arctic Ocean accounts for the 4.8 ~ 14.4 % of total amount of meltwater discharge to the world oceans during the BA period. This estimate is comparable those estimated by an ice sheet model for the onset of YD period in the maximum estimate (15%; Tarasov and Peliter, 2005), assuming

that about 1/7 of sea-level changes during the last deglacial period are due to meltwater from the Laurentide ice sheet.

This study indicated that a huge amount of meltwater was discharged to the Arctic Ocean. Nonetheless, the AMOC did not weaken during the BA period (Ritz et al., 2013), though it damped during the onset of the YD period. The following interpretations are possible; First, riverine freshwater was diluted by saltier water in the Canada Basin and did not impact the salinity of the North Atlantic during the BA period, while icebergs reached to the North Atlantic and reduced the salinity by melting during the onset of the YD period (Ritz et al., 2013; Keigwin et al., 2018). Second, the freshwater flux exceeded the critical level to damp the AMOC during the onset of the YD period, but not during the BA period. To answer these questions, quantitative estimates of freshwater discharge in the YD period is highly necessary.

In conclusion, the total volume of the K layer is estimated to be 917.5 km^3. This indicates 9.4 times higher sediment discharge than that of the present Mackenzie River. Rough-estimation indicates the freshwater discharge rate was 2 ~ 4 times higher than that of today. The total discharged water amount corresponds to a model estimate of the increased amount of sea water during the BA period. This water discharge did not seem to affect the AMOC.

4.4. General Summary

Radiocarbon dating of biogenic carbonates is widely used for marine sediments younger than the last 50,000 years, but not applicable to the sediments that do not contain carbonates. There is a method of substituting with bulk organic matter, but organic matter is complex of compounds of various ages, and the ^{14}C age of bulk organic matter is often older than the true age of sediment. In this study, we established a method to determine the sediment age by ramped pyrolysis of bulk organic matter. When sediments were pyrolyzed at elevated temperatures, the carbon of gas generated at higher temperatures in the same sample showed an older age. Samples with a large difference between the age of the sediment and the age obtained by ramped pyrolysis showed a large slope of the G1-G3 age with respect to the decomposition temperature. Based on this empirical relationship, a new calibration method was proposed to determine the dating age within 1600 years (average 300 years) for samples deposited in the past 15,000 years. This technique may be widely applied to the sediments that do not contain biogenic carbonates.

The post glacial period, 15,000 to 11,000 years ago, is characterized by a millennial-scale climate change. As a cause of this climate change, the hypothesis that the meltwater flowing out of the North American ice sheet changed the formation of the deep water in the North Atlantic and oscillated the Atlantic meridional ocean circulation. In this study,

we detected meltwater inflow events to the Arctic Ocean from deglaciation sediments in the western Arctic Ocean. The sedimentary structure, grain size distribution, mineral composition, organic carbon content, sulfur content, and tetraether lipid composition were analyzed for seven sediment cores collected from the western Arctic Ocean. A characteristic silt layer was observed in Chukchi Borderland. The sediment of this layer is rich in kaolinite, fine coal particles, and soil-derived tetraether lipids, and its provenance is assumed to be inland Canada where the kaolinite and coal-bearing Cretaceous Scholard Formation. The results of the ramped pyrolysis ^{14}C dating revealed that the lower limit of this layer was 14,500 years ago and the upper limit was 13,200 years ago. This period corresponds to the Bølling-Allerød warming period. The amounts of sediment and freshwater were estimated from the sedimentary area and thickness of the sediments that deposited by meltwater discharge event. The amount of meltwater calculated from the amount of sediment discharged during this period was equivalent to 5 ~ 14 % of the relative sea level change (25 m) at that time. However, this meltwater discharge did not affect the AMOC.

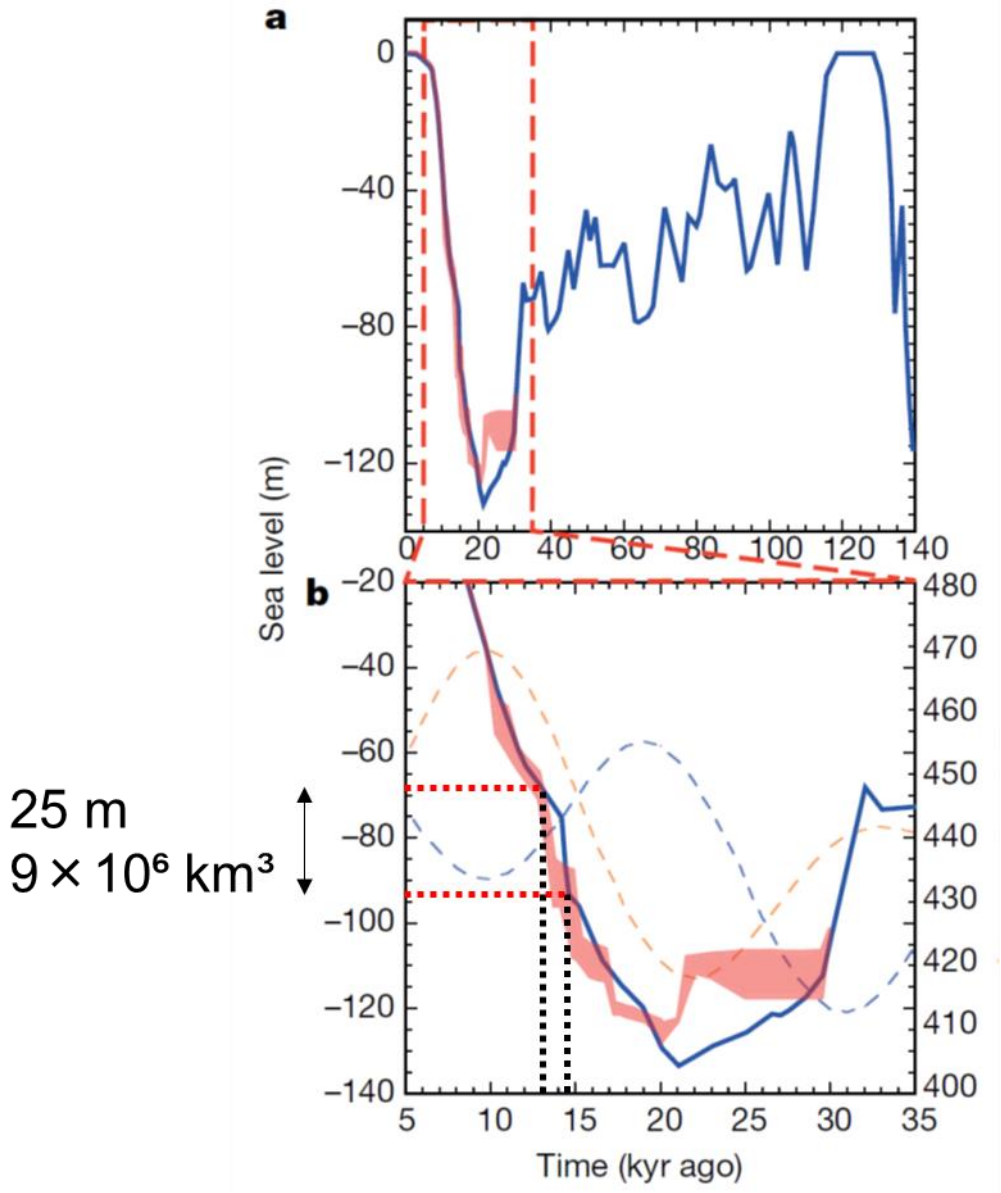

Fig. 4-1. Sea level changes during last 140 ka (a) and 5-35 ka (b) (Yokoyama et al., 2018). The dotted lines show the interval of BA period and sea level change.

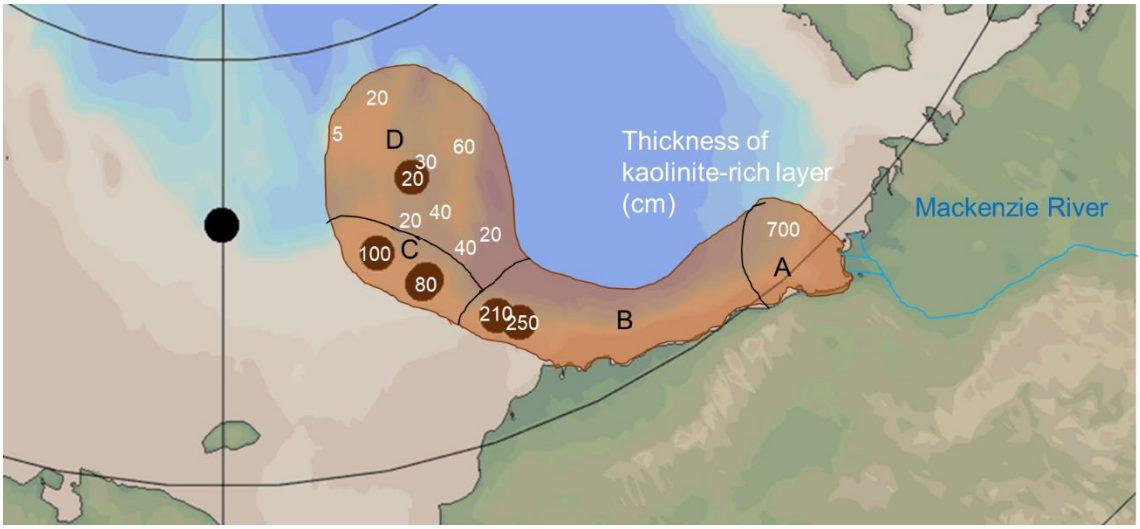

Fig. 4-2. Deposition area of the K1 layer in the western Arctic Ocean (brown shade). The numbers indicate the thickness of the K1 layer (cm). A: Mackenzie River Delta (5×10^4 km^2), B: Alaskan margin (1.4×10^5 km^2), C: Chukchi continental margin (5.5×10^4 km^2) and D: Chukchi borderland (1.9×10^5 km^2).

References

Andrews, J. T., Domack, E.W., Cunningham, W. L., Leventer, A., Licht, K. J., Jull, A. J. T., DeMaster, D. J., & Jennings A. E. (1999), Problems and possible solutions concerning radiocarbon dating of surface marine sediments, Ross Sea, Antarctica, *Quaternary Research*, *52*, 206–216.

Alley, R. B., Meeset, D. A., Shuman, C. A., Gow, A. J., Taylor, K. C., Grootes, P. M., White, J. W. C., Ram, M., Waddington, E. D., Mayewski, P. A., & Zielinski, G. A., (1993). Abrupt increase in Greenland snow accumulation at the end of the Younger Dryas event. *Nature*, *362*, 527.

Backman, J., Fornaciari, E., & Rio, D., (2009). Biochronology and paleoceanography of late Pleistocene and Holocene calcareous nannofossil abundances across the Arctic Basin. *Marine Micropaleontology*, *72*(1), 86-98.

Backman, J., Moran, K., & McInroy, D. (2005). IODP Expedition 302, Arctic Coring Expedition (ACEX): A first look at the Cenozoic paleoceanography of the central Arctic Ocean. *Scientific Drilling*, *1*, 12-17.

Belov, N. A., & Lapina, N. N. (1961). Donnye osadki Severnogo Ledovitogo okeana (Bottom Sediments of the Arctic Ocean). *Leningrad: Gidrometeoizdat.*

Benner, R., Benitez-Nelson, B., Kaiser, K., & Amon, R. M. (2004). Export of young

terrigenous dissolved organic carbon from rivers to the Arctic Ocean. *Geophysical Research Letters*, *31*(5), L05305.

Berner, R. A. (1982). Burial of organic carbon and pyrite sulfur in the modern ocean: its geochemical and environmental significance. *Am. J. Sci.;(United States)*, *282*.

Biscaye, P. E. (1964). Distinction between kaolinite and chlorite in recent sediments by X-ray diffraction. *American Mineralogist: Journal of Earth and Planetary Materials*, *49*(9-10), 1281-1289.

Bischof, J. F., Clark, D. L., & Vincent, J. S., (1996). Origin of ice‐rafted debris: Pleistocene paleoceanography in the western Arctic Ocean. *Paleoceanography*, *11*(6), 743-756.

Bischof, J. F., & Darby, D. A. (1997). Mid-to Late Pleistocene ice drift in the western Arctic Ocean: evidence for a different circulation in the past. *Science*, *277*(5322), 74-78.

Böhm, E., Lippold, J., Gutjahr, M., Frank, M., Blaser, P., Antz, B., Fohlmeister, J., Frank, N., Andersen, M. B., & Deininger, M., (2015). Strong and deep Atlantic meridional overturning circulation during the last glacial cycle. *Nature*, *517*(7532), 73-76.

Broecker, W. S., Kennett, J. P., Flower, B. P., Teller, J. T., Trumbore, S., Bonani, G., & Wolfli, W., (1989). Routing of meltwater from the Laurentide Ice Sheet during the

Younger Dryas cold episode. *Nature*, *341*, 318-321.

Burdige, D. J. (2007). Preservation of organic matter in marine sediments: controls, mechanisms, and an imbalance in sediment organic carbon budgets?. *Chemical reviews*, *107*(2), 467-485.

Carlson, A. E., Clark, P. U., Raisbeck, G. M., & Brook, E. J. (2007). Rapid Holocene deglaciation of the Labrador sector of the Laurentide Ice Sheet. *Journal of Climate*, *20*(20), 5126-5133.

Carson, M. A., Jasper, J. N., & Conly, F. M. (1998). Magnitude and sources of sediment input to the Mackenzie Delta, Northwest Territories, 1974–94. *Arctic*, 116-124.

Clark, D. L. (1970). Magnetic reversals and sedimentation rates in the Arctic Ocean. *Geological Society of America Bulletin*, *81*(10), 3129-3134.

Clark, D. L., Whitman, R. R., Morgan, K. A., & Mackey, S. D., (1980). Stratigraphy and glacial-marine sediments of the Amerasian Basin, central Arctic Ocean. *Geological Society of America Special Papers*, *181*, 1-65.

Coachman, L. K., & Aagaard, K. (1988). Transports through Bering Strait: Annual and interannual variability. *Journal of Geophysical Research: Oceans*, *93*(C12), 15535-15539.

Condron, A., & Winsor, P., (2012). Meltwater routing and the Younger Dryas.

Proceedings of the National Academy of Sciences, *109*(49), 19928-19933.

Dalrymple, R. W., & Maass, O. C. (1987). Clay mineralogy of late Cenozoic sediments in the CESAR cores, Alpha Ridge, central Arctic Ocean. *Canadian Journal of Earth Sciences*, *24*(8), 1562-1569.

Dansgaard, W., Johnsen, S. J., Clausen, H. B., Dahl-Jensen, D., Gundestrup, N. S., Hammer, C. U., Hvldberg, C. S., Steffensen, J. P., Svelnbjrnsdottir, A. E., Jouzel, J., & Bond, G., (1993). Evidence for general instability of past climate from a 250-kyr ice-core record. *Nature*, *364*(6434), 218-220.

Darby, D. A., Bischof, J. F., & Jones, G. A. (1997). Radiocarbon chronology of depositional regimes in the western Arctic Ocean. *Deep Sea Research Part II: Topical Studies in Oceanography*, *44*(8), 1745-1757.

Darby, D. A., Bischof, J. F., Spielhagen, R. F., Marshall, S. A., & Herman, S. W. (2002). Arctic ice export events and their potential impact on global climate during the late Pleistocene. *Paleoceanography*, *17*(2), 15-1.

Darby, D. A., Myers, W. B., Jakobsson, M., & Rigor, I. (2011). Modern dirty sea ice characteristics and sources: the role of anchor ice. *Journal of Geophysical Research: Oceans*, *116*(C9).

Darby, D. A., Ortiz, J., Polyak, L., Lund, S., Jakobsson, M., & Woodgate, R. A. (2009b).

The role of currents and sea ice in both slowly deposited central Arctic and rapidly deposited Chukchi–Alaskan margin sediments. *Global and Planetary Change*, *68*(1–2), 58–72.

Darby, D. A., Polyak, L., & Jakobsson, M. (2009a). The 2005 HOTRAX expedition to the Arctic Ocean. *Global and Planetary Change*, *68*(1–2), 1–4.

Domack, E. W., Jacobson, E. A., Shipp, S., & Anderson, J. B. (1999). Late Pleistocene–Holocene retreat of the West Antarctic Ice-Sheet system in the Ross Sea: Part 2—sedimentologic and stratigraphic signature. *Geological Society of America Bulletin*, *111*(10), 1517-1536.

Durand, B. (Ed.). (1980). *Kerogen: Insoluble organic matter from sedimentary rocks*. Editions technip.

Eglinton, T. I., Aluwihare, L. I., Bauer, J. E., Druffel, E. R., & McNichol, A. P. (1996). Gas chromatographic isolation of individual compounds from complex matrices for radiocarbon dating. *Analytical Chemistry*, *68*(5), 904–912.

Faux, J. F., Belicka, L. L., & Harvey, H. R. (2011). Organic sources and carbon sequestration in Holocene shelf sediments from the western Arctic Ocean. *Continental Shelf Research*, *31*(11), 1169-1179.

Flores, R.M., Stricker, G.D., & Kinney, S.A., (2003). Alaska coal resources and

coalbedmethane potential. *U.S. Geological Survey Bulletin*, 2198(10).

French, K. L., Hein, C. J., Haghipour, N., Wacker, L., Kudrass, H. R., Eglinton, T. I., & Galy, V. (2018). Millennial soil retention of terrestrial organic matter deposited in the Bengal Fan. *Scientific Reports*, *8*(1), 11997.

Gordeev, V. V., & Sidorov, I. S. (1993). Concentrations of major elements and their outflow into the Laptev Sea by the Lena River. *Marine Chemistry*, *43*(1-4), 33-45.

Guo, L., Semiletov, I., Gustafsson, Ö., Ingri, J., Andersson, P., Dudarev, O., & White, D. (2004). Characterization of Siberian Arctic coastal sediments: Implications for terrestrial organic carbon export. *Global Biogeochemical Cycles*, *18*(1), GB1036.

Hatcher, P. G., Spiker, E. C., Szeverenyi, N. M., & Maciel, G. E. (1983). Selective preservation and origin of petroleum-forming aquatic kerogen. *Nature*, *305*(5934), 498-501.

Hemingway, J. D., Rothman, D. H., Grant, K. E., Rosengard, S. Z., Eglinton, T. I., Derry, L. A., & Galy, V. V. (2019). Mineral protection regulates long-term global preservation of natural organic carbon. *Nature*, *570*(7760), 228-231.

Hopmans, E. C., Weijers, J. W., Schefuß, E., Herfort, L., Damsté, J. S. S., & Schouten, S. (2004). A novel proxy for terrestrial organic matter in sediments based on branched and isoprenoid tetraether lipids. *Earth and Planetary Science Letters*, *224*(1-2), 107-116.

Jakobsson, M., Løvlie, R., Al-Hanbali, H., Arnold, E., Backman, J., & Mörth, M. (2000). Manganese and color cycles in Arctic Ocean sediments constrain Pleistocene chronology. *Geology*, *28*(1), 23-26.

Jang, K., Han, Y., Huh, Y., Nam, S. I., Stein, R., Mackensen, A., & Matthiessen, J. (2013). Glacial freshwater discharge events recorded by authigenic neodymium isotopes in sediments from the Mendeleev Ridge, western Arctic Ocean. *Earth and Planetary Science Letters*, *369*, 148-157.

Keigwin, L. D., Klotsko, S., Zhao, N., Reilly, B., Giosan, L., & Driscoll, N. W. (2018). Deglacial floods in the Beaufort Sea preceded Younger Dryas cooling. *Nature Geoscience*, *11*(8), 599.

Kester, R. A., de Boer, W., & Laanbroek, H. J. (1996). Short exposure to acetylene to distinguish between nitrifier and denitrifier nitrous oxide production in soil and sediment samples. *FEMS microbiology ecology*, *20*(2), 111-120.

Kobayashi, D., Yamamoto, M., Irino, T., Nam, S. I., Park, Y. H., Harada, N., Nagashima, K., Chikita, K., & Saitoh, S. I. (2016). Distribution of detrital minerals and sediment color in western Arctic Ocean and northern Bering Sea sediments: Changes in the provenance of western Arctic Ocean sediments since the last glacial period. *Polar Science*, *10*(4), 519-531.

Krumbein, W. C. (1940). Flood gravel of San Gabriel Canyon, California. *Bulletin of the Geological Society of America*, *51*(5), 639-676.

Krylov, A. A., Andreeva, I. A., Vogt, C., Backman, J., Krupskaya, V. V., Grikurov, G. E., Moran, K., & Shoji, H. (2008). A shift in heavy and clay mineral provenance indicates a middle Miocene onset of a perennial sea ice cover in the Arctic Ocean. *Paleoceanography*, *23*(1).

Lisé-Pronovost, A., St-Onge, G., Brachfeld, S., Barletta, F., & Darby, D. (2009). Paleomagnetic constraints on the Holocene stratigraphy of the Arctic Alaskan margin. *Global and Planetary Change*, *68*(1–2), 85–99.

Manabe, S., & Stouffer, R. J. (1995). Simulation of abrupt climate change induced by freshwater input to the North Atlantic Ocean. *Nature*, *378*(6553), 165-167.

McGeehin, J., Burr, G. S., Jull, A. T., Reines, D., Gosse, J., Davis, P. T., Muhs, D., & Southon, J. R. (2001). Stepped-combustion ^{14}C dating of sediment: a comparison with established techniques. *Radiocarbon*, *43*(2A), 255-261.

McKay, J. L., de Vernal, A., Hillaire-Marcel, C., Not, C., Polyak, L., & Darby, D. (2008). Holocene fluctuations in Arctic sea-ice cover: dinocyst-based reconstructions for the eastern Chukchi Sea. *Canadian Journal of Earth Sciences*, *45*(11), 1377-1397.

Mullen, R. E., Darby, D. A., & Clark, D. L. (1972). Significance of atmospheric dust and

ice rafting for Arctic Ocean sediment. *Geological Society of America Bulletin*, *83*(1), 205-212.

Murton, J. B., Bateman, M. D., Dallimore, S. R., Teller, J. T., & Yang, Z. (2010). Identification of Younger Dryas outburst flood path from Lake Agassiz to the Arctic Ocean. *Nature*, *464*(7289), 740-743.

Naidu, A. S., & Mowatt, T. C., (1984). Sources and dispersal patterns of clay minerals in surface sediments from the continental-shelf areas off Alaska. *Geological Society of America Bulletin, 94*(7), 841–854.

Oeschger, H., Welten, M., Eicher, U., Moll, M., Riesen, T., Siegenthaler, U., & Wegrnuller, S., (1980). ^{14}C and other parameters during the Younger Dryas cold phase. *Radiocarbon*, *22*(2), 299-310.

O'Regan, M. (2007). Data report: high-resolution bulk density, dry density, and porosity records from the Arctic Coring Expedition, IODP Expedition 302. In *Proc. IODP| Volume* (Vol. 302, p. 2).

Ortiz, J. D., Polyak, L., Grebmeier, J. M., Darby, D., Eberl, D. D., Naidu, S., & Nof, D. (2009). Provenance of Holocene sediment on the Chukchi-Alaskan margin based on combined diffuse spectral reflectance and quantitative X-Ray Diffraction analysis. *Global and Planetary Change*, *68*(1–2), 73–84.

Park, K., Ohkushi, K. I., Cho, H. G., & Khim, B. K. (2017). Lithostratigraphy and paleoceanography in the Chukchi Rise of the western Arctic Ocean since the last glacial period. *Polar Science*, *11*, 42–53.

Park, Y. H., Yamamoto, M., Nam, S. I., Irino, T., Polyak, L., Harada, N., Nagashima, K., Khim, B. K., Chikita, K., & Saitoh, S. I. (2014). Distribution, source and transportation of glycerol dialkyl glycerol tetraethers in surface sediments from the western Arctic Ocean and the northern Bering Sea. *Marine Chemistry*, *165*, 10-24.

Parsons, J. D., Bush, J. W., & Syvitski, J. P. (2001). Hyperpycnal plume formation from riverine outflows with small sediment concentrations. *Sedimentology*, *48*(2), 465-478.

Pearce, C., Varhelyi, A., Wastegård, S., Muschitiello, F., Barrientos, N., O'Regan, M., Cronin, T. M., Gemery, L., Semiletov, I., Backman, J., & Jakobsson, M. (2017). The 3.6 ka Aniakchak tephra in the Arctic Ocean: a constraint on the Holocene radiocarbon reservoir age in the Chukchi Sea. *Climate of the Past*, *13*(4), 303.Pearson, A., Eglinton, T. I., & McNichol, A. P. (2000). An organic tracer for surface ocean radiocarbon. *Paleoceanography*, *15*(5), 541-550.

Pearson, A., McNichol, A. P., Benitez-Nelson, B. C., Hayes, J. M., & Eglinton, T. I. (2001). Origins of lipid biomarkers in Santa Monica Basin surface sediment: a case study using compound-specific Δ14C analysis. *Geochimica et Cosmochimica Acta*, *65*(18), 3123-

3137.

Peterse, F., van der Meer, J., Schouten, S., Weijers, J. W., Fierer, N., Jackson, R. B., ... & Damsté, J. S. S. (2012). Revised calibration of the MBT–CBT paleotemperature proxy based on branched tetraether membrane lipids in surface soils. *Geochimica et Cosmochimica Acta*, *96*, 215-229.

Petrov, P. Y., Semikhatov, M. A., & Sergeev, V. N. (1995). Development of the Riphean carbonate platform and distribution of silicified microfossils: the Sukhaya Tunguska Formation, Turukhansk Uplift, Siberia. *Stratigraphy and Geological Correlation*, *3*(6), 602-620.

Phillips, R. L., & Grantz, A., (2001). Regional variations in provenance and abundance of ice-drifted clasts in Arctic Ocean sediments: implications for the configuration of Late Quaternary oceanic and atmospheric circulation in the Arctic. *Marine Geology, 172,* 91–115.

Polyak, L., Curry, W. B., Darby, D. A., Bischof, J., & Cronin, T. M., (2004). Contrasting glacial/interglacial regimes in the western Arctic Ocean as exemplified by a sedimentary record from the Mendeleev Ridge. *Palaeogeography, Palaeoclimatology, Palaeoecology, 203*(1), 73–93.

Polyak, L., Darby, D. A., Bischof, J. F., & Jakobsson, M. (2007). Stratigraphic constraints

on late Pleistocene glacial erosion and deglaciation of the Chukchi margin, Arctic Ocean. *Quaternary Research*, *67*(2), 234-245.

Polyak, L., Bischof, J., Ortiz, J. D., Darby, D. A., Channell, J. E., Xuan, C., Kaufman, D. S., Løvlie, R., Schneider, D. A., Eberl, D. D., Adler, R. E., & Council, E. A., (2009). Late Quaternary stratigraphy and sedimentation patterns in the western Arctic Ocean. *Global and Planetary Change*, *68*(1), 5–17.

Polyak, L., Belt, S. T., Cabedo-Sanz, P., Yamamoto, M., & Park, Y. H. (2016). Holocene sea-ice conditions and circulation at the Chukchi-Alaskan margin, Arctic Ocean, inferred from biomarker proxies. *The Holocene*, *26*(11), 1810-1821.

Poore, R. Z., Osterman, L., Curry, W. B., & Phillips, R. L. (1999). Late Pleistocene and Holocene meltwater events in the western Arctic Ocean. *Geology*, *27*(8), 759-762.

Rachold, V., Eicken, H., Gordeev, V. V., Grigoriev, M. N., Hubberten, H. W., Lisitzin, A. P., Shevchenko, V. P., & Schirrmeister, L. (2004). Modern terrigenous organic carbon input to the Arctic Ocean. In *The organic carbon cycle in the Arctic Ocean* (pp. 33-55). Springer, Berlin, Heidelberg.

Rahmstorf, S., (1997). Risk of sea-change in the Atlantic. *Nature*, *388*(6645), 825.

Rahmstorf, S., (2002). Ocean circulation and climate during the past 120,000 years. *Nature*, *419*(6903), 207-214.

Rahmstorf, S., (2003). Timing of abrupt climate change: A precise clock. *Geophysical Research Letters*, *30*(10), 1510.

Reimer, P. J., Bard, E., Bayliss, A., Beck, J. W., Blackwell, P. G., Ramsey, C. B., Buck, C. E., Cheng, H., Edwards, R. L., Friedrich, M., Grootes, P. M., Guilderson, T. P., Haflidason, H., Hajdas, I., Hatte, C., Heaton, T. J., Hoffmann, D. L., Hogg, A. G., Hughen, K.A., Kaiser, K. F., Kromer, B., Manning, S. W., Niu, M., Reimer, R. W., Richards, D. A., Scott, E. M., Southon, J. R., Staff, R. A., Turney, C. S. M., & van der Plicht, J. (2013). IntCal13 and Marine13 radiocarbon age calibration curves 0–50,000 years cal BP. *Radiocarbon*, *55*(4), 1869-1887.

Ritz, S. P., Stocker, T. F., Grimalt, J. O., Menviel, L., & Timmermann, A. (2013). Estimated strength of the Atlantic overturning circulation during the last deglaciation. *Nature geoscience*, *6*(3), 208.

Rosenheim, B. E., Day, M. B., Domack, E., Schrum, H., Benthien, A., & Hayes, J. M. (2008). Antarctic sediment chronology by programmed-temperature pyrolysis: Methodology and data treatment. *Geochemistry, Geophysics, Geosystems*, *9*(4), Q04005.

Rosenheim, B. E., Santoro, J. A., Gunter, M., & Domack, E. W. (2013). Improving Antarctic sediment ^{14}C dating using ramped pyrolysis: An example from the Hugo

Island trough. *Radiocarbon*, *55*(1), 115–126.

Ruddiman, W. F., (2001). *Earth's Climate: past and future*. Macmillan, 465P.

Seierstad, I. K., Abbott, P. M., Bigler, M., Blunier, T., Bourne, A. J., Brook, E., Buchardt, S. L., Buizert, C., Clausen, H. B., Cook, E., Dahl-Jensen, D., Davis, S. M., Guillevic, M., Johnsen, S. J., Pedersen, D. S., Popp, T. J., Rasmussen, S. O., Severinghaus, J. P., & Vinther, B. M. (2014). Consistently dated records from the Greenland GRIP, GISP2 and NGRIP ice cores for the past 104 ka reveal regional millennial-scale $\delta^{18}O$ gradients with possible Heinrich event imprint. *Quaternary Science Reviews*, *106*, 29-46.

Stein, R., 2008. Arctic ocean sediments: processes, proxies, and palaeoenvironment. In: Dev. Mar. Geol, vol. 2. Elsevier, Amsterdam, pp. 1–587.

Stein, R., Matthiessen, J., Niessen, F., Krylov, A., Nam, S. I., & Bazhenova, E. (2010). Towards a better (litho-) stratigraphy and reconstruction of Quaternary paleoenvironment in the Amerasian Basin (Arctic Ocean). *Polarforschung*, *79*(2), 97-121.

Stokes, C. R., Clark, C. D., Darby, D. A., & Hodgson, D. A. (2005). Late Pleistocene ice export events into the Arctic ocean from the M'Clure strait ice stream, Canadian Arctic Archipelago. *Global and Planetary Change*, *49*(3-4), 139-162.

Subt, C., Fangman, K. A., Wellner, J. S., & Rosenheim, B. E. (2016). Sediment

chronology in Antarctic deglacial sediments: Reconciling organic carbon ^{14}C ages to carbonate ^{14}C ages using Ramped PyrOx. *The Holocene*, *26*(2), 265–273.

Subt, C., Yoon, H. I., Yoo, K. C., Lee, J. I., Leventer, A., Domack, E. W., & Rosenheim, B. E. (2017). Sub-ice shelf sediment geochronology utilizing novel radiocarbon methodology for highly detrital sediments. *Geochemistry, Geophysics, Geosystems*, *18*(4), 1404–1418.

Tarasov, L., & Peltier, W. R. (2004). A geophysically constrained large ensemble analysis of the deglacial history of the North American ice-sheet complex. *Quaternary Science Reviews*, *23*(3-4), 359-388.

Trettin, H. P. (Ed.). (1991). *Geology of the Innuitian orogen and arctic platform of Canada and Greenland*. Geological Society of America.

The Atlas of Canada, (2009). Natural Resources Canada, *National Atlas of Canada*, sixth edition.

Tissot, B., & Welte, D. H. (1978). *Petroleum occurrence and formation.* Springer, 699P.

Weijers, J. W., Schouten, S., van den Donker, J. C., Hopmans, E. C., & Damsté, J. S. S. (2007). Environmental controls on bacterial tetraether membrane lipid distribution in soils. *Geochimica et Cosmochimica Acta*, *71*(3), 703-713.

Williams, C., Flower, B. & Hastings, D. W. (2012). Seasonal Laurentide ice sheet melting

during the ‘Mystery Interval’ (17.5–14.5 ka). *Geology*, *40*, 955–958.

Williams, E. K., Rosenheim, B. E., McNichol, A. P. & Masiello, C. A. (2014). Charring and non-additive chemical reactions during ramped pyrolysis: applications to the characterization of sedimentary and soil organic material. *Organic Geochemistry*, *77*, 106–114.

Yamamoto, M., & Polyak, L., (2009). Changes in terrestrial organic matter input to the Mendeleev Ridge, western Arctic Ocean, during the Late Quaternary. *Global and Planetary Change*, *68*(1), 30-37.

Yamamoto, M., Nam, S. I., Polyak, L., Kobayashi, D., Suzuki, K., Irino, T., & Shimada, K. (2017). Holocene dynamics in the Bering Strait inflow to the Arctic and the Beaufort Gyre circulation based on sedimentary records from the Chukchi Sea. *Climate of the Past*, *13*(9), 1111-1127.

Yamamoto, M., Okino, T., Sugisaki, S., & Sakamoto, T. (2008). Late Pleistocene changes in terrestrial biomarkers in sediments from the central Arctic Ocean. *Organic Geochemistry*, *39*(6), 754-763.

Yokoyama, Y., Esat, T. M., Thompson, W. G., Thomas, A. L., Webster, J. M., Miyairi, Y., Sawada, C., Aze, T., Matsuzaki, H., Okuno, J., Fallon, S., Braga, J. C., Humblet, M., Iryu, Y., Potts, D. C., Fujita, K., Suzuki, A., & Kan, H. (2018). Rapid glaciation and a

two-step sea level plunge into the Last Glacial Maximum. *Nature*, *559*(7715), 603.

Zhang, T., Wang, R., Polyak, L., & Xiao, W. (2019). Enhanced deposition of coal fragments at the Chukchi margin, western Arctic Ocean: Implications for deglacial drainage history from the Laurentide Ice Sheet. *Quaternary Science Reviews*, *218*, 281-292.